8-11-2020

Experimental study of breathers and rogue waves generated by random waves over non-uniform bathymetry

A. Ludu
Embry-Riddle Aeronautical University, ludua@erau.edu

A. Wang
Dalian University of Technology

Z. Zong
Dalian University of Technology

L. Zou
Dalian University of Technology

Y. Pei
Dalian University of Technology

Scholarly Commons Citation

A. Wang, A. Ludu, Z. Zong, L. Zou, Y. Pei; Experimental study of breathers and rogue waves generated by random waves over non-uniform bathymetry. Physics of Fluids 1 August 2020; 32 (8): 087109. https://doi.org/10.1063/5.0016379

RESEARCH ARTICLE | AUGUST 11 2020

Experimental study of breathers and rogue waves generated by random waves over non-uniform bathymetry

A. Wang (王爱民) ; A. Ludu ; Z. Zong (宗智) ; L. Zou (邹丽); Y. Pei (裴玉国)

Physics of Fluids 32, 087109 (2020)
https://doi.org/10.1063/5.0016379

Physics of Fluids ARTICLE scitation.org/journal/phf

Experimental study of breathers and rogue waves generated by random waves over non-uniform bathymetry

Cite as: Phys. Fluids 32, 087109 (2020); doi: 10.1063/5.0016379
Submitted: 4 June 2020 • Accepted: 20 July 2020 •
Published Online: 11 August 2020

A. Wang (王爱民),[1,a] A. Ludu,[2,b] Z. Zong (宗智),[1,3,c] L. Zou (邹丽),[1,4,d] and Y. Pei (裴玉国)[1,e]

AFFILIATIONS

[1]School of Naval Architecture, Dalian University of Technology, Dalian 116024, Liaoning, China
[2]Department of Mathematics & Wave Laboratory, Embry-Riddle Aeronautical University, Daytona Beach, Florida 32114, USA
[3]Collaborative Center of Advanced Ships and Deep-water Engineering, DUT, Dalian 116024, Liaoning, China
[4]State Key Laboratory of Structural Analysis for Industrial Equipment, DUT, Dalian 116024, Liaoning, China

[a]**Electronic mail:** wam@mail.dlut.edu.cn
[b]**Author to whom correspondence should be addressed:** ludua@erau.edu
[c]**Electronic mail:** zongzhi@dlut.edu.cn. **Also at**: Liaoning Deep-Water Floating Structure Engineering Technology Lab, Dalian, Liaoning, China.
[d]**Electronic addresses:** lizou@dlut.edu.cn and zoulidut@126.com. **Also at:** Collaborative Innovation Center for Advanced Ship and Deep-Sea Exploration, Shanghai 200240, People's Republic of China.
[e]**Electronic mail:** ygpei@dlut.edu.cn

ABSTRACT

We present experimental evidence of formation and persistence of localized waves, breathers, and solitons, occurring in a random sea state and uniformly traveling over non-uniform bathymetry. Recent studies suggest connections between breather dynamics and irregular sea states and between extreme wave formation and breathers, random sea states, or non-uniform bathymetry individually. In this paper, we investigate the joint connection between these phenomena, and we found that breathers and deep-water solitons can persist in more complex environments. Three different sets of significant heights have been generated within a Joint North Sea Wave Observation Project wave spectrum, and the wave heights were recorded with gauges in a wave tank. Statistical analysis was applied to the experimental data, including the space and time distribution of kurtosis, skewness, Benjamin–Feir index, moving Fourier spectra, and probability distribution of wave heights. Stable wave packages formed out of the random wave field and traveling over shoals, valleys, and slopes were compared with exact solutions of the nonlinear Schrödinger equation with a good match, demonstrating that these localized waves have the same structure as deep-water breathers. We identify the formation of rogue waves at moments and over regions where the kurtosis and skewness have local maxima. These results provide insights for understanding of the robustness of Peregrine and higher-order Akhmediev breathers, Kuznetsov–Ma solitons, and rogue waves, and their occurrence in realistic oceanic conditions, and may motivate analogous studies in other fields of physics to identify limitations of exact weakly nonlinear models in non-homogeneous media.

I. INTRODUCTION

It is very important to predict with greatest accuracy ocean waves for the safety of ships and offshore structures, especially when operating in rough sea conditions where extreme events could arise. Ocean extreme waves, also known as rogue waves (RWs), occur without apparent warning and have a disastrous impact, mainly because of their large wave heights.[1,2] These highly destructive phenomena have been observed frequently enough to justify advanced studies. Possible candidates to explain the formation of RWs in the ocean are presently under intense discussion.[3,4] This topic attracted recently a great deal of scientific interest not only because of the

accurate modeling and prediction of these extremes and similar structures[2,5,6] but also because of the interdisciplinary nature of the weakly nonlinear localized waves present in nonlinear dispersive media.[7,8] Explanations solely based on linear wave dynamical theories (constructive interference of multiple small amplitude waves) cannot grasp the nonlinear coupling between modes, a phenomenon that becomes important when the amplitude of the waves increases. A successful approach for the nonlinear surface gravity localized wave propagation and RW formation explanation is the modulation instability (MI).[8] Such a phenomenon can be described by the evolution of an unstable wave packet that absorbs energy from neighbor waves and increases its amplitude, reaches a maximum, and then transfers its energy back to the other waves.[9] The mathematical model for such unstable modes is the nonlinear Schrödinger (NLS) equation[7,10–12] or modified versions of it [modified NLS (MNLS)].[13,14] Exact solutions of the NLS equation provide feasible models that were successfully used to provide deterministic numerical and laboratory prototypes both to reveal novel insights of MI[15] and to describe RW.[16] The reason for the efficiency of the NLS model is that through its balance between nonlinearity and linear dispersion, it can describe well the occurrence of Benjamin–Feir instability and the associated nonlinear wave dynamics.[17] Experimental studies confirmed the validity of the NLS for deep-water waves.[18] One other advantage of using the NLS is its integrability[19] and the analytic form for solutions, especially useful when compared to experimental results. In NLS models, the instability corresponds to various breather solutions of this equation.[12] The NLS equation is characterized by a richer family of coherent structures, namely breather solutions.[3,9,10,14,20–22] Even if the breathers change their shape during their evolution and hence are not traveling solitons, they maintain their identity against perturbations and collisions. Breathers are exact solutions of the nonlinear Schrödinger equation (NLS)[7,12] and describe the dynamics of modulation unstable Stokes waves[23] in deep water.[2,24] Some of the exact solutions for the NLS equation are rational expressions of hyperbolic and trigonometric functions of space and time and are known as Akhmediev breathers (ABs).[25] The AB solutions are space-periodic models to study the Benjamin–Feir MI initiated by periodic modulation of Stokes waves.[8] Infinitesimal perturbation of the periodic carrier wave grows exponentially and after reaching a highest amplitude decays back in the background wave field.[11] Another commonly used model solution, a limiting situation for the AB for an infinite modulation period, is a rational function called the Peregrine breather (PB).[8,25,26] In addition to modeling the Benjamin–Feir MI, the NLS equation has time-periodic solutions in the form of envelope solitons traveling on a finite background of ocean waves of various frequencies, with the algebraic growth rate larger than three.[11] These solutions not corresponding to the MI phenomenon, so the unexpectedness is not their feature, are called Kuznetsov–Ma (KM) solitons.[7,27] Both AB and PB have been considered as possible ocean RW models,[28] and their features have been investigated experimentally and numerically.[18,29,30]

It is natural to apply such successful NLS breather deep-water models in realistic oceanographic situations where the underlying field is irregular and random.[31] Even if initially the ocean surface dynamics is narrow-banded, winds, swell,[32] currents, and wave breaking may induce strong irregularities. Recently, the possibility of extending NLS models to such broad-banded processes was demonstrated, a fact that becomes valuable in the prediction of extreme events and in extending the range of applicability of coherent structures in ocean engineering.[4,9] There has been a lot of progress lately in this direction,[9,10,14,22] both in numerical and experimental analyses. Recently, by using integrable turbulence theory, the appearance of RW in a chaotic wave state was demonstrated.[33] In Ref. 34, the possibility for exact breather solutions to trigger extreme events in realistic oceanic conditions was reported. By embedding the PB into an irregular ocean configuration with random phases, for example, a JONSWAP spectrum,[34] the unstable PB wave packet perturbation initiates the focusing of an extreme event of RW type, in good agreement with NLS and even modified NLS (MNLS) predictions.[10] In this study, rigorous numerical simulations based on the fully nonlinear enhanced spectral boundary integral method show that weakly nonlinear localized PB-type packets propagate in random seas for a long enough time, within a certain range of steepness and spectral bandwidth of the nonlinear dynamical process, somehow in opposition to what the weakly nonlinear theory for narrow-banded wave trains with moderate steepness would predict. These results are also backed up by recent hydrodynamic laboratory experiments, which also show that PB breathers persist even under wind forcing.[31] In the last decade, the dynamics of gravity waves and their statistical properties while traveling over non-uniform bathymetry were considered as an enhancing factor for generation of solitons, breathers, and RWs. Both experimental and numerical studies were involved, including Korteweg–de Vries (KdV) models,[35] MNLS and Boussinesq models,[36] or fully nonlinear flow solvers.[37,38] Trulsen *et al.* showed[36] that the change in the depth can provoke increased likelihood of RWs as waves propagate from deeper to shallower water. In these shallower regions, the linear refraction induces shorter wavelength, while the amplitude and the steepness become larger. The study of the dependence on the depth h of some of the statistical parameters [spectrum, variance, skewness, kurtosis, Benjamin–Feir index (BFI), etc.] for long unidirectional waves over a flat bottom shows the existence of interactions between several competing processes within the nonlinear waves. On the one hand, Whitham theory for nonlinear waves predicts that in shallower bathymetry, long-crested waves become modulationally stable; hence, MI tends to decrease with the decrease in kh, and actually, it annihilates when $kh < 1.363$ because the coefficient of the cubic nonlinear term in the NLS vanishes at this threshold.[39] On the other hand, the Zakharov equation[36] predicts the increase in MI through the increase in the wave steepness ε by linear refraction and by static nonlinear second-order effects with the decrease in the depth. Numerical studies by Xia *et al.*[40] have shown that shallower water involves the decrease of kurtosis all together by these effects. Numerical studies of the NLS performed by Lawrence *et al.*[41] show that the combination of focusing and nonlinear effects result in increase of kurtosis when waves run over shallower depths, for example, when kh: $20 \rightarrow 0.2$. The same strong non-Gaussian deviation toward a shallower bottom was confirmed in numerical studies by Tian *et al.*[35] More interesting though, the change in waves' kurtosis with the depth depends on what side of the slope the waves are investigated. In experiments over a sloped bottom, Trulsen *et al.*[36] showed that waves propagating over a sloping bottom from a deeper to a shallower domain present a local maximum of kurtosis and skewness close to the shallower side of the slope and a local maximum of probability of a large wave envelope at the same location,

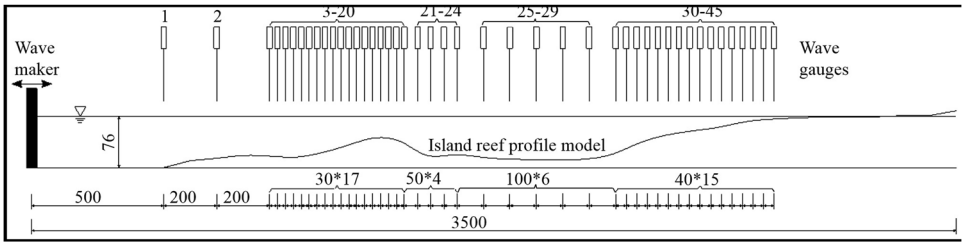

FIG. 1. Experiment measurement setup. Positions of the wave gauges with respect to the wave maker and bottom topography. The upper numbers are gauge numbers, and the bottom numbers represent centimeters, e.g., 30 ∗ 17 means 17 gauges separated equidistantly by 30 cm.

that can generate a local maximum of RW formation probability at that point, results backed by NLS numerical solutions in Ref. 42. In the present work, we provide a detailed analysis of experimental data obtained in a wave tank concerning the occurrence of breathers, solitons, and RWs out of a random wave field and their survival over non-uniform bathymetry. In our analysis, we rely on the individual successful modeling or observation of RW occurrence from breathers and solitons,[28] confirmations of the occurrence of RWs from random sea states,[4,9] the occurrence of breathers and solitons from random sea states,[10,32,34,35,43] or breather and soliton occurrence from non-uniform bathymetry.[36–38,42] Our goal is to present the survival of such localized traveling coherent structures through a random wave field and over non-uniform bathymetry simultaneously, a new configuration not yet investigated to our present knowledge. Nonlinear localized waves over non-uniform bathymetry have a different dynamical behavior. The nonlinear waves reach an equilibrium at some depth, but they tend to lose this equilibrium when traveling over different depths, and it takes time and space extension for the waves to reach another state of equilibrium. Our experimental measurements provide evidence of the numerical predictions for long-crested waves propagating over non-uniform bathymetry described above and also confirm the experimental results obtained by Trulsen *et al.* in Ref. 36. This paper is organized as follows: In Sec. II, we present the experimental setup, the types of waves and physical parameters we generated, and how the time series were collected and analyzed. In Sec. III, we analyze the experimental results with respect to the wave steepness, the Ursell number, and MI characteristics such as the BFI, skewness, kurtosis, Fourier spectra, and wave heights that condition the formation and persistence of breathers, solitons, and RWs. In Sec. IV, we present the NLS theoretical formalism for a flat bottom and MNLS for non-uniform depth and compare our experimental results with the corresponding PB, AB, and higher-order breathers and KM solitons, and we also determine the limits of applicability of these exact models to deep-water random waves over non-uniform bathymetry.

II. EXPERIMENTAL SETUP FOR RANDOM WAVE GENERATION OVER NON-UNIFORM BATHYMETRY

The experiments have been performed in the wave tank of the State Key Laboratory of Coastal and Offshore Engineering in Dalian University of Technology. The wave tank is L_{tank} = 50 m long, 3 m wide, and 1 m deep. The wave tank is provided with a hydraulic servo wave maker, which can generate waves of arbitrary shape with a minimum period of 0.66 s at 15 cm wave maximum height. An absorbing beach is installed at the opposite end to avoid wave reflections (Fig. 1). In the experiments described in this paper, the bottom has non-uniform shape with the maximum depth of water in the tank h = 0.76 m. To ensure a unidirectional wave field and long-crested waves, the wave tank was divided in two sections along its length: one of 2 m wide with non-uniform bathymetry and one with flat bottom of 1 m wide for reference. A number of 45 resistive wave probes (gauges) were aligned along the wave propagation direction to measure the wave height. The surface height of the water at these specified positions is measured with an accuracy of up to six significant digits at a sampling δt = 0.02 s, with 170 s time

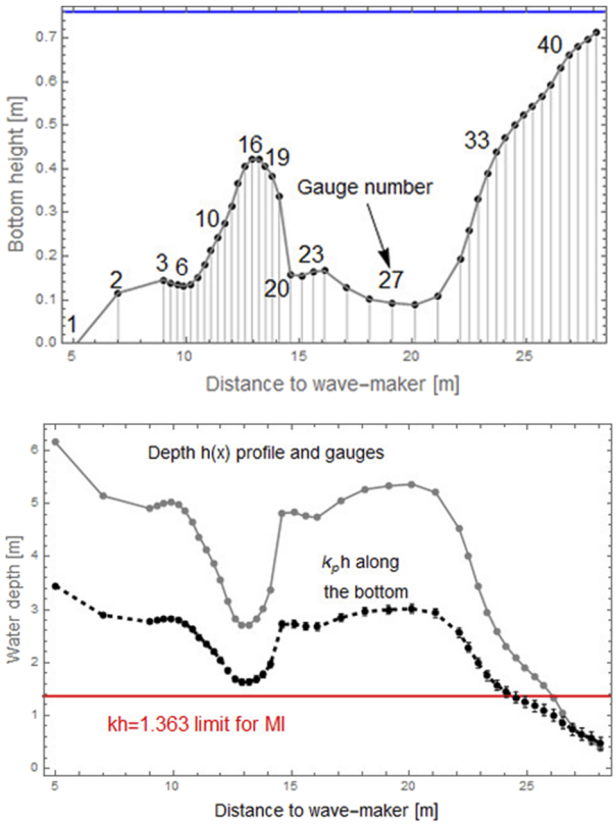

FIG. 2. (Top) Bathymetry profile in the wave tank, placement of some key gauges, and the quiescent water level (blue line). (Bottom) Water depth $h(x)$ (gray solid line), expression $k_p(x)h(x)$ (black dotted line with error bars), and MI extinction threshold 1.363 (red line).

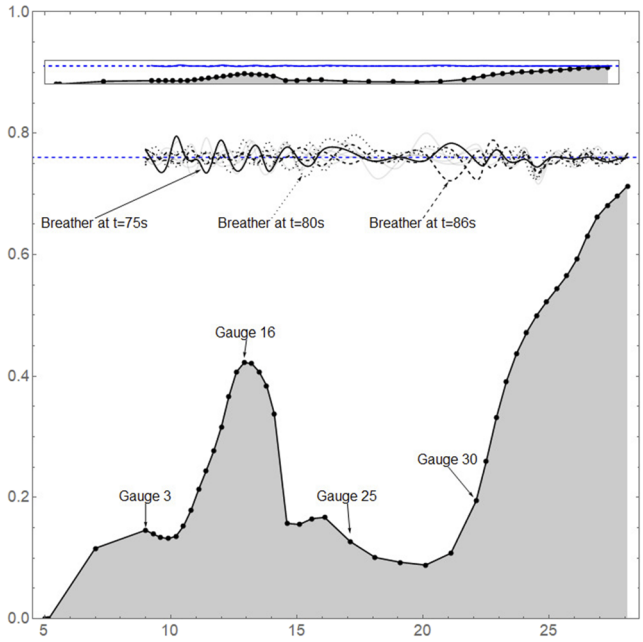

FIG. 3. Longitudinal section in the wave tank with variable bathymetry. The wave maker is at the left of the frame, the dots represent gauges, and the vertical axis shows depth in meters. The quiescent water level is the blue dashed line, and several of our waves are presented to visualize relations between the specific wave heights, wavelengths, and depth. We chose moments t = 75 s (solid line), 80 s (dotted line), and 86 s (dashed line) when coherent spontaneous structures (matched with Peregrine breathers) form over gauge numbers 5 and 6 (solid line), 24–27 (dotted line), and 30–34 (dashed line), respectively. In the upper inset, the same picture is present at real scale.

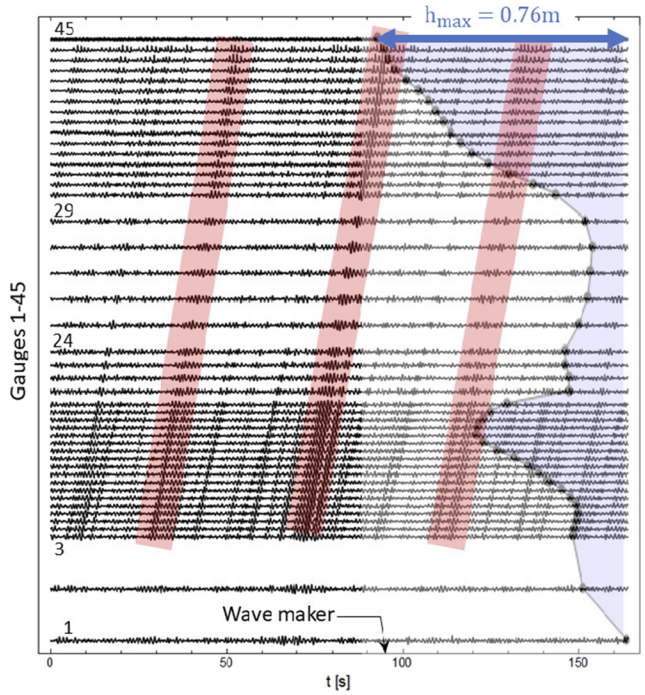

FIG. 4. Random wave field of significant wave height H_s = 3.22 cm, significant period T_s = 0.95 s, and variable bottom with depth $h \leq 0.76$ m. The horizontal axis is time evolution (0 s–160 s), and the 45 gauge signals (Nos. 1, 3, 24, 29, and 45 indicated in the figure) are lined up along the vertical axis from the wave maker (bottom) to the run-up (zero water depth on top of the frame). The blue shape represents the bottom profile, which is artificially overlapped in the figure for visual reference, and the dots placed on it represent the gauge positions. We identify at least three coherent, stable, and almost uniformly traveling packages, highlighted with red stripes.

series length memory. The gauges are placed as shown in Figs. 1–4, namely: first two control gauges, beginning at 9 m from the wave maker, then 17 equidistant gauges with 30 cm separation, then four gauges with 50 cm separation, then six gauges separated by 1 m each, and finally, 16 gauges separated by 40 m. Since the width of the basin is large compared with the characteristic wavelength of our experiments, viscous energy dissipation that occurs mostly on sidewalls is assumed to be negligible at the center of the basin where our wave probes are located.[14]

The bottom shape is inspired by some specific sea floor bathymetry. At the wave maker end, the bottom is deep and then gradually increases its heights toward a shoal where we have a minimum depth h_{min} = 0.34 m at gauge 16 at x = 13 m from the wave maker. From this point, the bottom height drops at a larger slope and it reaches its deepest region at x = 20 m at gauge 28. Then, the bottom gradually becomes shallower, increasing its height toward a run-up beach all the way to the water surface (see Figs. 1–4). We have carried 40 different experiments by changing the significant wave height H_s and significant period T_s (see Table I), but in order to keep a reasonable article length, we present here only one T_s value and three relevant cases of H_s. The duration of time series recorded for all cases $B1$–$B4$, J was 171 s. The JONSWAP spectrum was chosen for the irregular wave simulation, described by the following parameters:[44]

$$S(f) = \frac{\beta_J H_s^2 \gamma^{\delta}}{T_p^4 f^5} \mathrm{Exp}\left[-\frac{1.25}{(T_p f)^4}\right], \tag{1}$$

$$\delta = \mathrm{Exp}\left[-\frac{\left(\frac{f}{f_p}-1\right)^2}{2\sigma^2}\right], \tag{2}$$

TABLE I. Experimental settings and parameters.

Case	H_s (cm)	T_s (s)
B1	3.22	0.95, 1.03, 1.23, 1.32, 1.41, 1.51
B2	5.20	The same
B3	6.20	The same
B4	1.60; 2; 3; 4; 5; 6; 7; 8	1.23
J	5.20; 7.18; 9.20	0.75
	3.22; 5.20; 7.18; 9.20	0.85
	3.22; 6.20; 8.20; 9.20	0.95

with

$$\beta_J \simeq \frac{0.062\,38(1.094 - 0.019\,15\ln\gamma)}{0.230 + 0.0336\gamma - 0.185(1.9+\gamma)^{-1}}, \tag{3}$$

$$T_p \simeq \frac{T_s}{1 - 0.132(\gamma+0.2)^{-0.559}}, \tag{4}$$

and the function of wave frequency given by

$$\sigma = \begin{cases} 0.07, & f \le f_p \\ 0.09, & f > f_p, \end{cases}$$

where f_p is the spectrum peak frequency, T_p is the spectrum peak frequency, T_s is the significant period, and γ is the spectrum peak elevation parameter, which we set $\gamma = 3.3$. Given the geometry of the tank and dynamics of the wave maker, ranges of the random wave parameters are limited by three physical constraints: deep-water condition,[45] neglecting capillary waves, and giving the waves enough room to form breathers and eventually rogue waves. These constraints request $\lambda_{capillary} < \lambda < \min\{L_{tank}, 2\pi h\}$. The wave number for the carrier wave k_p is derived from the linear dispersion relation $k_p = 4\pi^2/(gT_p^2)$. Under these constraints and according to the parameters chosen in Table I, the range of peak wavelength that can be excited in the tank becomes 0.85 m $< \lambda_p <$ 3.55 m.

In our experiments, the wavelength and group velocity of the carrier wave slightly change along the tank because of the non-uniform bottom. In the deep regions at gauge 2–7 and 22–29 (h = 0.65 m–0.76 m) or at x = 5 m–12 m and 14 m–22 m from the wave maker (see Figs. 2 and 3), we have for the carrier wave period T_p = 0.95 s, deep-water long-waves with parameters λ_p = 1.407 m, k_p = 4.49 m^{-1}, and v_g = 0.76 m/s. In the intermediate region over the shoal ($h \simeq$ 0.35 m) at gauge 11–19 or at x = 12 m–14 m from the wave maker, we still have deep-water long-waves with parameters λ_p = 1.31 m, k_p = 4.79 m^{-1}, and v_g = 0.85 m/s. Only toward the right end of the beach ($h \ge$ 0.2 m) at gauge 36–45 or at $x >$ 25 m from the wave maker, we have shallow water and waves with parameters λ_p = 1.13 m, k_p = 5.55 m^{-1}, and v_g = 0.89 m/s. In the upper frame of Fig. 2, we present the bathymetry and gauge placement. In the bottom frame, we present also with respect to the distance to the wave maker, the water depth h and the calculated values of $k_p h$ depending on the depth and corresponding wavelength for fixed T_p. It appears that everywhere along the tank, the condition[1,7,8,46] for developing MI is fulfilled, $k_p h > 1.363$; the deep-water NLS equation model is valid for the self-focusing regime of solutions; and wave train modulations will experience exponential growth (see, for example, Figs. 7 and 8).

The physical parameters that characterize the evolution of irregular waves are characteristic wave steepness $\varepsilon_p = k_p H_s/2$, which in our experiments is ranged between 0.015 and 0.33, and the bandwidth. The spectral bandwidth is determined by choosing the peak enhancement factor, which in our case of γ = 3.3 induces $\Delta f/f_p$ = 0.095. The Benjamin–Feir index (BFI) for the theory of Stokes waves,[8,9] which measures the nonlinear and dispersive effects of wave groups, is given by

$$\mathrm{BFI} = \frac{\varepsilon_p f_p}{\sqrt{2}\Delta f}. \tag{5}$$

Beyond a critical value of BFI = 1,[14] an irregular wave field is expected to be unstable and wave focusing can occur. In our experiments, we can cover the range 0.11 < BFI < 2.2, namely, covering all types of sea, from linear waves to stronger MI with development of a rogue sea state, especially since the total length of the measurements covers 28 m, which is larger than the distance over which the MI is expected to appear.[14] Since the waves in our experiments may enter occasionally into a strongly nonlinear wave regime, the NLS equation may provide only a very good fit with these experiments, as we will see in Sec. IV. We first consider irregular JONSWAP waves with significant wave height H_s = 3.22 cm and significant period T_s = 0.95 s over this complex bathymetry.

In Fig. 3, we present a typical experimental result. In this vertical longitudinal section of the wave tank with variable bathymetry (the gray shape at the bottom) and a wave maker placed at the left of the frame, we show the level of quiescent water by a blue dashed line, on which we overlapped several waves obtained at t = 75 (solid line showing a nonlinear coherent wave package on top of the shoal), at 80 s (dotted line showing the same structure that traveled now over the deepest valley), and at t = 86 s (dashed line, when the same coherent package travels up the slope of the run-up). The behavior of the waves shown in Fig. 3 is in agreement with the Djorddjevićć–Redekopp model for deep water with variable bathymetry, using a modified NLS equation with variable coefficients,[46] as we will notice later [Eq. (15)]. Indeed, in all our experiments, the amplitudes and wavelengths of the waves slightly decrease, while v_g slightly increases, over the shoaling region (about gauge 16), and the

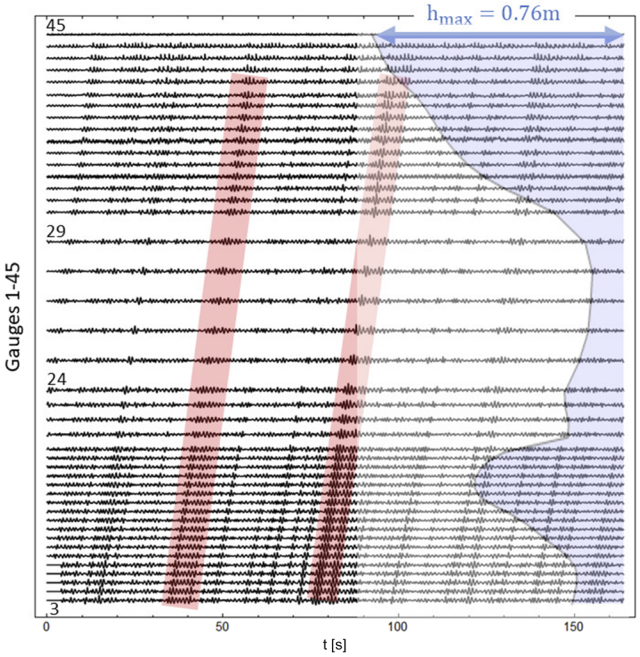

FIG. 5. Same configuration and parameters as in Fig. 4, except here H_s = 5.2 cm. We still identify at least two coherent and stable traveling packages, highlighted with red stripes.

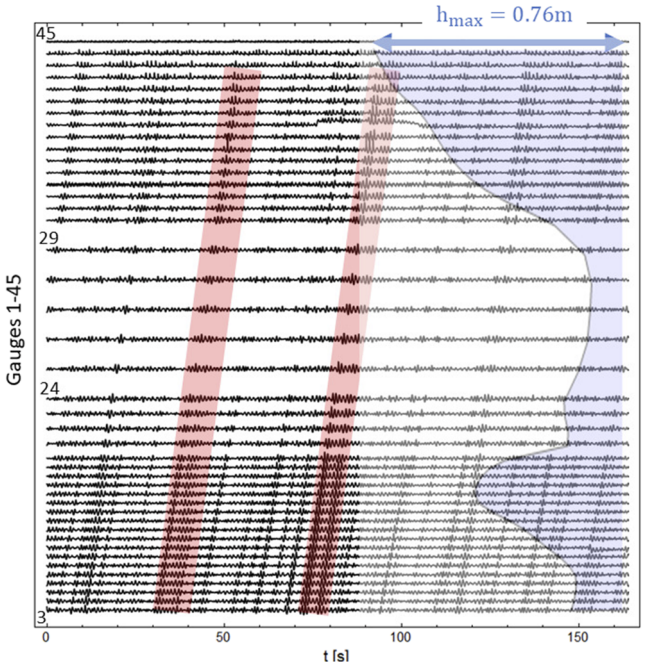

FIG. 6. Same configuration and parameters as in Fig. 4, except here H_s = 6.2 cm. We still identify at least two coherent and stable traveling packages, highlighted with red stripes.

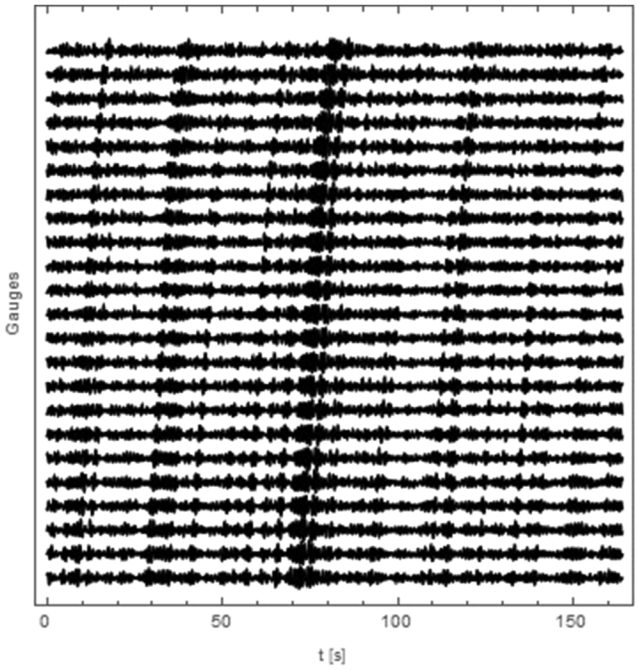

FIG. 7. Time series of gauge 3–23 for T_p = 0.9 s and H_s = 3.22 cm in the region where gauges are equidistant but run over the shoal. The coherent structures, possible breathers, appear traveling with stable shape and group velocity (slope of the line of traveling patterns representing the wave packages) over the variable bathymetry.

situation reverses when waves advance over deeper regions (gauges 27–29).

In the upper inset of Fig. 3, we present the longitudinal section at real scale, and the same waves, to stress that all our wave amplitudes are negligible compared to the variations in bathymetry. For every experiment of generation of random waves, we noted the formation of some localized traveling coherent wave packages. These structures, once formed, keep traveling with almost the same group velocity over the variable bathymetry over the shoal and tend to disintegrate when the kh = 1.363 criterion for MI is not fulfilled anymore, which is around gauge Nos. 39–41. In Figs. 4–6, we present such an example of a 164 s long time series (horizontal axis time) as measured by different gauges whose outputs are stacked along the vertical axis. The traveling coherent structures (three of them, for example) are highlighted in red stripes in the figure, and the bathymetry shape is artificially overlapped in the figure for visual reference. These coherent wave packages propagate approximately uniformly with the peak group velocity of order $v_g \simeq 0.815$ m/s.

A larger image for such a typical time series only for gauges 1–23 is given in Fig. 7 where one can detect better the occurrence and stability over the shoal of the nonlinear coherent packages: one begins at t = 27 s and another larger one begins at t = 68 s. In Fig. 8, we present in more extended detail wave profiles for H_s = 3.22 cm and 160 s duration time series measured at five locations (gauges 1, 2, 23, 30, and 41) to observe better the nonlinear coherent formations that are spontaneously formed in the random waves and that travel for as long as 20 m.

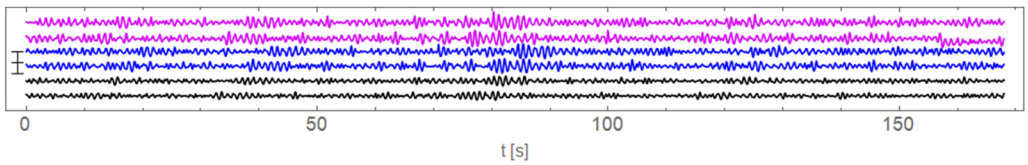

FIG. 8. Steepness effect on coherent wave packages. The wave profiles from gauge 10 (at x = 11.1 m) and 20 (at x = 14.1 m) for three cases: H_s = 3.22 cm (first two bottom signals, black signals), H_s = 5.2 cm (middle two signals, blue signals), and H_s = 6.2 cm (upper two, magenta signals) vs time. Coherent wave packages, most likely Peregrine breathers, are spontaneously formed in the random waves and can be observed traveling for as long as 20 m. Vertical tick on the left represents 20 cm wave height.

III. ANALYSIS OF EXPERIMENTAL RESULTS

In the analysis of our experiments over variable bathymetry, we follow the approach of Trulsen *et al.*,[36,42,47] by performing statistics over the time series (and not over the space wave field) for the determination of the reference wave and to discern the extreme waves or other coherent structures. In this procedure, $H_s = H_s(x)$ becomes a function of space, and the criteria for identifying breather solutions or RWs become local. This approach, supported by numerical studies,[38,42] allows us to isolate the situation favorable for initiation of RW because linear refraction itself at variable bathymetry points cannot change the probability of RW unless such local criteria for RW are not employed.[36] Random long-crested waves were propagated over the non-uniform bathymetry. The slope of the bathymetry is 1:10 at the beginning of the shoal (gauge 3), followed by a sudden drop −1:240 (gauge 19), and then followed by a region of oscillating slopes between −1:16 and +1:16. After gauge 28, we have a raising beach with slope ranging from 1:35 at gauge 30 to 1:10 over its last 5 m. The gauges are placed as shown in Figs. 1–4. Three cases of long-crested random waves were generated with different nominal significant wave heights H_s and constant nominal peak periods T_p, as shown in Table I. The peak wave number k_p has been computed from the linear wave dispersion relation $\omega_p^2 = gk_p \tanh k_p h$, where $\omega_p = 2\pi/T_p$, $g = 9.81$ m/s^2. The characteristic amplitude is calculated as in Ref. 36 as $a_c = H_s/\sqrt{8}$ corresponding to a uniform wave of the same mean power. The Ursell number is $U_r = k_p a_c/(k_p h)^3$.

The three H_s cases for 45 recording gauges times 8192 samples taken at $\delta t = 0.02$ s intervals minus the startup effects provide about 7000 peak periods, which provide sufficiently reasonable estimates of kurtosis, skewness, and overall distribution functions.[36] In Table II, we present some wave parameters for the three H_s cases investigated and for four regions of bathymetry, namely, deep water, the deepest region, shoal, and toward the upper parts of the run-up beach. In all these regions, the NLS theory derived by Zakharov[12] applies and the MI develops in all cases with $k_p h > 1.363$ for the self-focusing regime. The steepness is $\varepsilon = k_p a_c$, and the Ursell number was also calculated for all the cases (Table II), and it shows a very good agreement with the similar cases investigated in Ref. 36. U_r has a small value in almost all deep regions, with moderate increased values above the shoal but still in the range of Stokes third and NLS equation modeling, and larger values of U_r above the beach where the waves cannot be considered anymore nonlinear deep water, and the character shifts from Stokes fourth to fifth order to cnoidal behavior, toward breakers in the end of the slope. In shallower water, the second-order nonlinearity of KdV dynamics becomes responsible for the strong correlation observed between skewness, kurtosis, and U_r (see also Fig. 16).

Some further insight into understanding the waves obtained in these experiments can be obtained by looking at the wave spectrum at different positions along the wave tank. The spectra at five representative points for the three cases of significant wave heights are shown in Fig. 9 with linear scales. The signal peaks and the Fourier spectra were obtained by using automatic multiscale peak detection based on the Savitzky–Golay method. All the nominal peaks are centered around the carrier frequency $T_p = 0.9$ s. There is a slight spectral development leading to a downshift of the peak, but not very visible, which means that the MI is present almost all over the measurements, except the last few gauges. The spectra corresponding to the deeper sides independently if this deep region was before and after the shoal are almost identical (solid lines in Fig. 9). The spectra of waves on top of the shoal (dashed line) and the spectra at gauges on the ramp about the same height as the shoal (dotted line) are not too different from the deep region ones. However, visible changes in the spectrum show when the waves propagate toward more shallower regions on the final beach (gray line). At these points, where skewness and kurtosis attain maximum values (see Fig. 10), the spectrum tends to show a second maximum around frequencies doubling the carrier frequency, most likely because of the growth of second-order bound harmonics caused by the increased nonlinearity at shallower depth. Further into the shallow region, the spectrum significantly broadens and becomes noisier since energy is shared to lower and higher frequencies. This situation becomes evident for regions with $k_p h \geq 1.363$ in agreement with the results obtained in Refs. 36 and 38.

Nonlinear transfer of energy between modes gives rise to deviations from statistical normality of random waves (e.g., Gaussian). The most convenient statistical properties intended to characterize nonlinear coherent wave packages or extreme wave occurrence are the third- and fourth-order moments of the free surface elevation $\eta(x, t)$,[36,38] namely, the skewness and the kurtosis defined as

$$\text{skewness} = \lambda_3 = \frac{\langle \eta - \langle \eta \rangle^3 \rangle}{\sigma^3},$$

$$\text{kurtosis} = \lambda_4 = \frac{\langle \eta - \langle \eta \rangle^4 \rangle}{\sigma^4} = \frac{\langle \eta^4 \rangle}{3\langle \eta^2 \rangle^2} - 1,$$

where $\langle , \rangle$ stands for the average over time and σ is the standard deviation of η, directly related to the significant wave height $H_s = 4\sigma$.

TABLE II. Three significant heights at following depths: deep (gauges 3–7, 22–24, and 30), deepest (gauges 26–28), shoal (gauges 15–18), and beach (gauges 42–44).

$T_p = 0.95$ s	Deep $h = 0.6$ m $k_p h = 2.7$		Deepest $h = 0.66$ m $k_p h = 3$		Shoal $h = 0.33$ m $k_p h = 1.6$		Beach $h = 0.2$ m $k_p h = 1.1$	
H_s (cm)	$k_p a_c$	U_r	$k_p a_c$	U_r	$k_p a_c$	U_r	$k_p a_c$	U_r
3.22	0.055	0.29	0.051	0.21	0.055	1.3	0.063	4.6
5.2	0.083	0.47	0.082	0.35	0.089	2.4	0.103	7.5
6.2	0.098	0.56	0.097	0.41	0.106	2.9	0.123	9

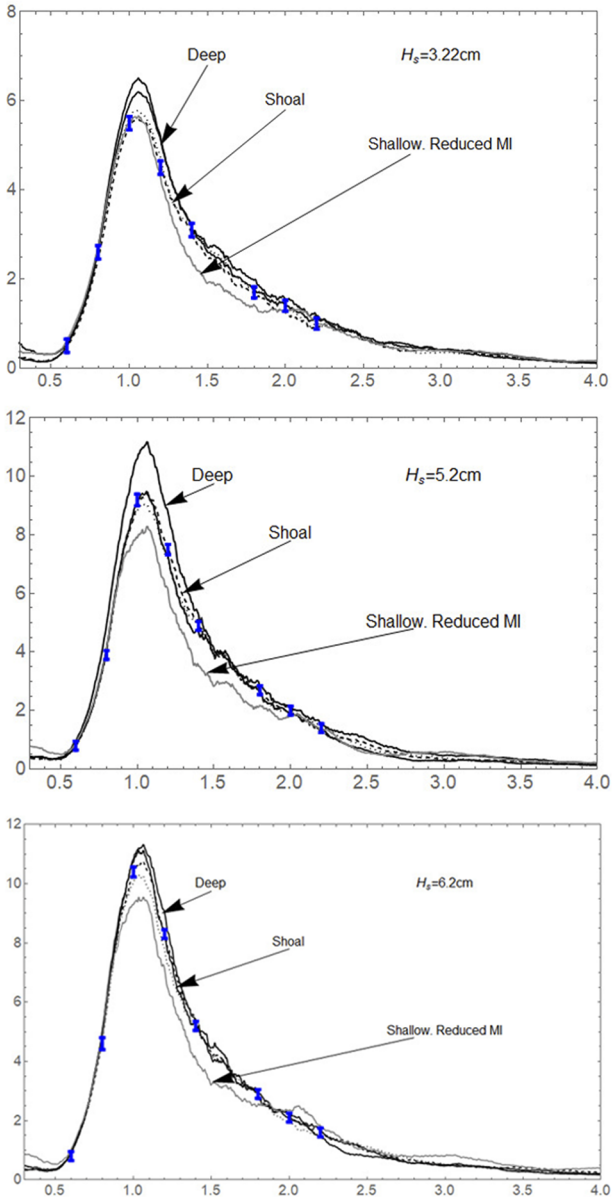

FIG. 9. Linear scale Fourier spectra for H_s = 3.22 cm (upper frame), H_s = 5.2 cm (middle frame), and H_s = 6.2 cm (bottom frame), all at T_p = 0.95 s, for five representative points at gauge Nos. 5, 11, 16, 22, and 39. The spectrum for the deeper sides before and after the shoal is represented with a solid line; the spectra of waves on top of the shoal are presented with a dashed line; the spectra at gauges on the ramp about the same height as the shoal is presented with a dotted line, and the spectra for regions with $k_ph \geq 1.363$ are presented with gray lines. Error bars (blue) are added at the spectra for the top of shoal (dashed line) where errors are maximal.

The skewness characterizes the asymmetry of the distribution with respect to the mean, while the kurtosis measures the importance of the tails. The kurtosis of the wave field is a relevant parameter in the detection of extreme sea states.[40]

In Fig. 10, we present the kurtosis of the surface elevation in the left frame and the skewness of the surface elevation in the right frame for the three significant wave heights experimented. The statistical estimates indicate 98% confidence intervals obtained from 16 500 selected samples from the original data.

For smaller wave amplitudes, there is a local maximum of kurtosis and skewness on top of the shallower edge of the shoal. For larger amplitude waves, this kurtosis local maximum shifts toward the beginning of the slope, toward the deeper region. All waves of all heights record a global maximum of the kurtosis in the deepest region, over gauges 24–30, similar to the numerical simulations in Refs. 35 and 41 and experiments described in Refs. 36, 42, and 47. This effect is related to the fact that deeper means kh greater than 1.363, as given in Table II, and is also related to the spectral evolution leading to a slight downshift of the shallow spectrum with dotted, dashed, and gray lines in Fig. 9. For all cases, the global maximum of these two statistical quantities is most prominent at the beginning of the shoal, that is, at the positive slope edges of the shoals. In all three cases of different H_s values representing different steepness degrees of the waves, except the end of the run-up beach, the depth is everywhere larger than the threshold value for MI, and no significant shift of the spectral peak can be easily seen.

Over deep-water regions with $kh \geq 1.363$, higher initial BFI (like the waves with H_s = 5.2 cm or 6.2 cm; see the red and blue upper curves in Fig. 14), the kurtosis tends to be stabilized at higher values, as can be seen in the left column in Fig. 10 for x = 3 m–8 m and x = 25 m–30 m, for waves with H_s = 3.22 cm, for x = 7 m–10 m and x = 25 m–28 m, for waves with H_s = 5.2 cm, and for waves with H_s = 6.2 cm. This result agrees well with previous publications, demonstrating that stabilized kurtosis is larger in deep water and smaller in shallower water.[42]

However, when $kh \to 1.363$ beginning at $x \simeq 35$ m, nonlinear effects diminish and the kurtosis decreases toward 3. This is also visible in Fig. 10: for smaller steepness waves with H_s = 3.22 cm, kurtosis tends to drop slightly around $x \simeq 36$ m just before the gray vertical stripe in the figure. The dropping effect is more visible at higher steepness, H_s = 5.2 cm at 36 m, and again less intense for the steepest waves, H_s = 6.2 cm. After the 1.363 threshold, the observed oscillations in kurtosis and skewness may be generated by other shallow water effects, Bragg effect, reflection, or linear diffraction. Our results make evident that when a wave field travels over a bottom slope into shallower water, a wake-like structure may be anticipated on the shallower side for the skewness and the kurtosis, as was previously confirmed in Ref. 42. The general expressions for the skewness and the kurtosis of the deep-water surface evaluated with Krasitskii's canonical transformation in the Hamiltonian[40] apply to our cases with $\varepsilon \simeq 0.1$ (shallower regions for H_s = 5.2 cm and all regions for H_s = 6.2 cm; see Table II), and our experimental results line up well with this theory when correlating the values of kurtosis and skewness from Fig. 10 with the k_ph values from Fig. 2 (bottom).

Noting that the value of the BFI decreases with the decrease in the water depth, as we can see it happening for $x > 23$ m (or after gauge 33) in Fig. 14, while the nonlinear coherent structures (which we identified with Peregrine or higher-order NLS breathers) keep propagating stably up to shallow water regions, we infer that the probability of RWs occurring near the edge of a continental shelf may exhibit a different spatial structure than for wave fields entering from deep sea and BFI deep-water criteria may not apply the same

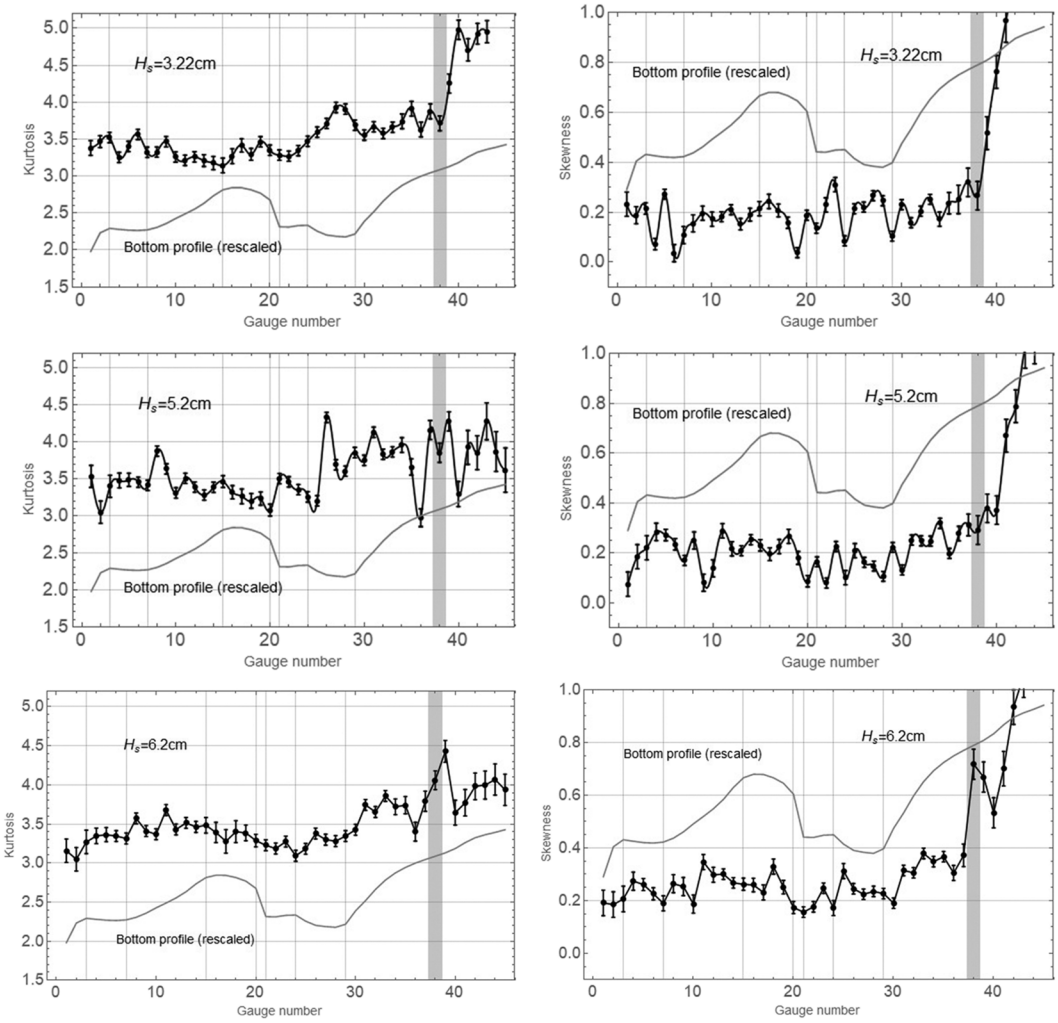

FIG. 10. Kurtosis (left frames) and skewness (right frames) plotted vs the gauge number, next to the re-scaled bottom profile (solid line). The upper row represents the waves with H_s = 3.22 cm; the middle row represents steeper waves with H_s = 5.2 cm; and the bottom row represents the steepest waves with H_s = 6.2 cm. All have the same T_p = 0.95 s, and the wave maker is to the left. The vertical grid lines separate different regimes, namely, deep, slope, shoal, quick drop, deep bottom, the deepest, and the run-up beach. The thick gray vertical band represents the position x where MI theoretically vanishes, i.e., $kh \to 1.363$. Error bars are included.

way. In addition to the analysis of the BFI vs position, bathymetry, and the slope of bathymetry in Fig. 14, we also present in Fig. 15 a distribution of the BFI vs time for a selection of gauges (positions in the tank). Even early in the setting of nonlinear wave packages in the first 16 s, the BFI values are manifestly larger (~1.3, the gray curves) at the positions and moments where the localized packages (breathers) travel through, compared to the BFI values (~0.2 to 0.5) for the rest of the random wave field (the solid blue background). We will discuss in more detail the space–time distribution of BFI in Sec. IV A.

Right after the shoal, both the kurtosis and skewness show oscillations in the values because of a combination between nonlinear effects and linear refraction. One interesting observation resulting from Fig. 10 is that for small steepness $\varepsilon < 0.08$ waves, the kurtosis and skewness are larger above the extreme depths h (very deep or $h \simeq h_{max}$ or very shallow or $h \ll h_{max}$), while for larger steepness waves, these two statistical moments tend to acquire their largest values above the sloppy regions of the bottom. This observation can be expressed in a phenomenological relation of the form

$$\lambda_{3,4} \sim C_1\left(h - \frac{h_{max}}{2}\right)^2 + \varepsilon C_2\left|\frac{dh}{dx}\right| \tag{6}$$

for some empirically determined constants $C_{1,2}$. The conclusions obtained from our experimental results and our statistical analysis of kurtosis and skewness coincide with the statistical behavior suggested in the numerical studies from Ref. 38 and with the experimental results obtained for sloped bottom in Ref. 36. We

have thus shown that as waves propagate over a shoal and variable bathymetry in general, local maxima in kurtosis and skewness occur closer to the beginning and to the end of the slope, mainly on the shallower side of the slope.[35] These regions can provide larger probability for the formation of high-amplitude breathers,[41,42] multiple breathers, or higher-order breathers, and possibly RW formation.[47]

A. Rogue waves from random background

In deep-water, long-crested waves are subject to MI,[8,11] which is known to generate conditions for RW formation.[2,7,10,11,28,46,48] It was also found that nonlinear modulations during the evolution of irregular waves cause spectral development and frequency down-shift, suspected to be related to the occurrence of RW.[36,49] In this subsection, we investigate the occurrence of higher amplitude waves, out of the random background, as candidates for RWs.

Extreme height waves isolated in time and space from the typical background reference wave field is considered to be a RW if it satisfies some common criteria such as $\eta/H_s > 1.25$ or $H/H_s > 2$, where η is the crest elevation and H is the wave height.[36] In Fig. 11, we present an example of two time series recorded in our experiments at two locations, 19 m (left frame) and 26.5 m (right frame) from the wave maker. The vertical axis shows the wave amplitude $\eta(t)$ normalized to the characteristic wave height $H_s = 3.22$ cm. We recorded such large amplitudes at 19 m, 22 m, 23.5 m, and 26.5 m (gauges 27, 30, 33, and 41, respectively) from the wave maker. The horizontal grid lines represent, in the order of their heights, minimum surface (blue), standard deviation (black), and maximum wave (red). The maximum height recorded is $2.1–2.42H_s$, which qualifies them as RWs. These events happen over the deep-water parts at the locations where kurtosis and skewness have local maxima (Fig. 10).

For a system composed of a large number of independent waves, such as the random generation, the surface elevation is expected to be described by a Gaussian probability density function. Under this hypothesis, Longuet-Higgins[9,20,21] showed that if the wave spectrum is narrow banded, then the probability distribution of crest-to-trough wave heights is given by the Rayleigh distribution. The distribution was found to agree well with many field observations.[9] Nevertheless, recently,[20,21] it was shown numerically and theoretically that if the ratio between the wave steepness and the spectral bandwidth (BFI) is large, a departure from the Rayleigh distribution is observed. This departure from the Rayleigh distribution was attributed to the MI mechanism. Moreover, from numerical simulations of the NLS equation, it was found[9] that, as a result of the MI, oscillating coherent structures may be excited from random spectra. In our experiments, we obtained a very good correlation between the waves at regions and during time intervals producing a narrower width spectrum and the corresponding detection (at the same locations and moments of time) of coherent stable, traveling structures, most likely NLS breathers (AB, KM, and Peregrine of higher-order breathers; Sec. IV).

In Figs. 12 and 13, we present examples of Fourier spectra in the time-frequency domain calculated with a 4 s moving window at different locations and different moments of time. In these figures, the combined relative errors from wave profile measurements and numerical evaluation do not exceed 5%. In these figures, the red curves represent narrower bandwidth wave spectra measured at points where also the coherent packages were detected and assimilated with breathers/solitons/RWs, wave packages described in Sec. III. Namely, the red curves in Figs. 12 and 13

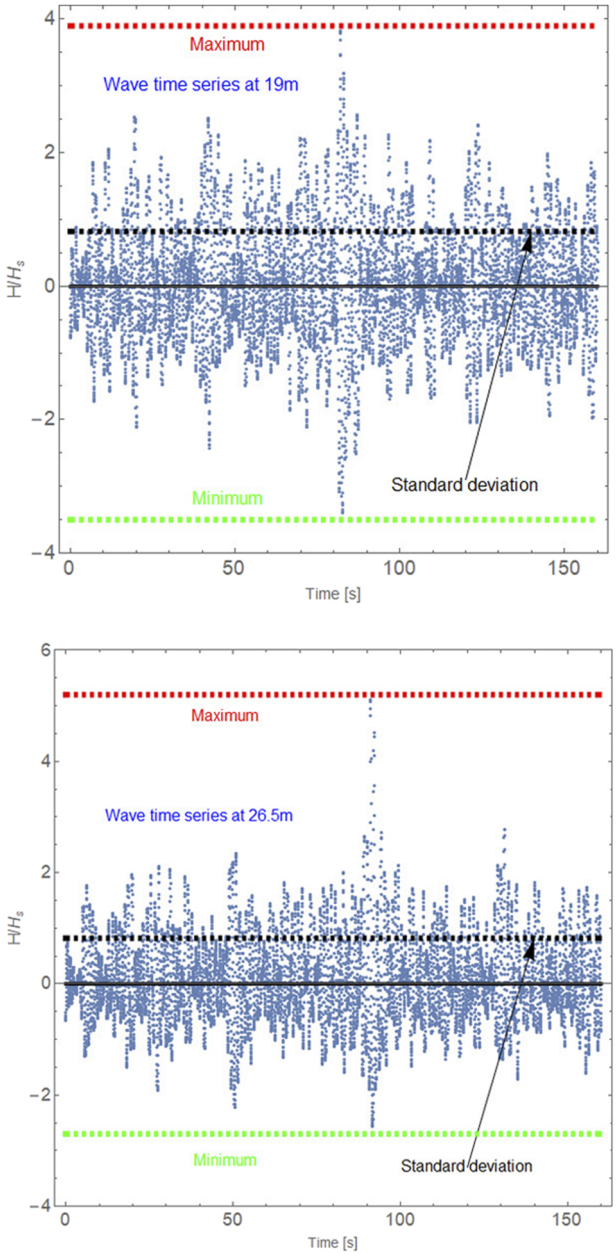

FIG. 11. Time series of the recorded wave amplitudes $\eta(t)$ normalized to their characteristic wave height $H_s = 3.22$ cm, measured at 19 m and 26.5 m (gauge 27 and 41). The horizontal grid lines represent, from bottom to top, the minimum surface (blue), standard deviation (black), and maximum wave (red). The maximum height recorded is $2.1–2.42H_s$, which qualifies them as RWs.

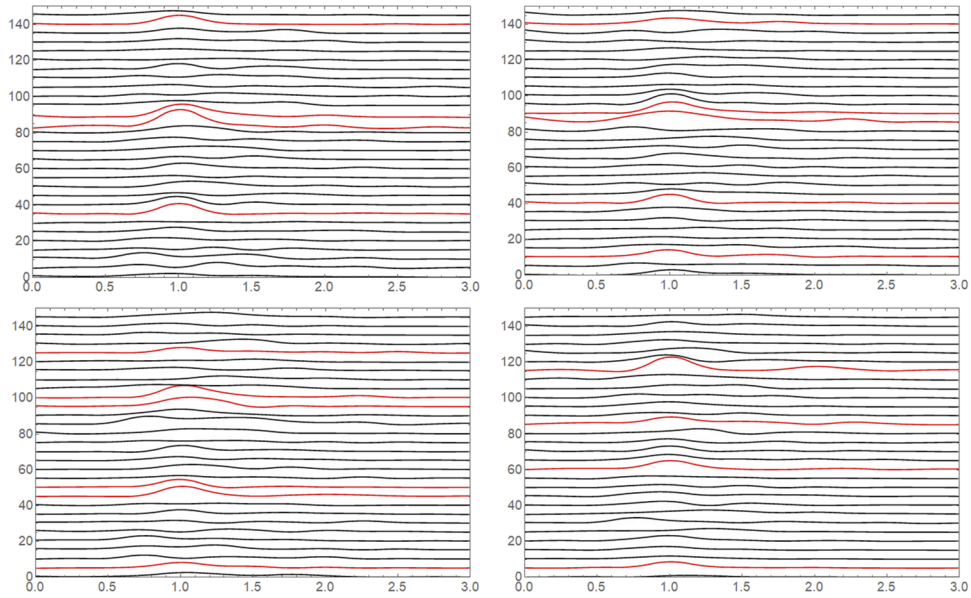

FIG. 12. Moving Fourier spectra in the time–frequency domain, calculated at different moments with a 4 s integration window for H_s = 3.22 cm. The spectra are ordered vertically vs the moment of time they are centered. The horizontal axis represents frequency in Hz. From the left upper corner CW, the frames represent spectra of waves measured at gauge 3 (at 9 m), 10 (at 12 m), 23 (at 14.1 m), and 41 (at 22.1 m). The selected red curves are taken at moments and points where localized stable packages were detected and assimilated with breathers/solitons/RWs: these spectra have obviously narrower bandwidths.

coincide with a good coefficient of correlation (c = 0.76 Pearson correlation) with the structures highlighted with red stripes in Figs. 4–6 and with the coherent packages in uniform motion identified in the mapping of Figs. 7, 8, 19, and 20; they also coincide with the packages chosen for theoretical match with breathers, shown in Figs. 21 and 23–25, and they are closely related to the extreme amplitude waves shown in Fig. 11.

These positive correlations represent the evidence that the MI process takes place in our experimental real long-crested water waves, with high values for the BFI index (the ratio between the wave steepness and the spectral bandwidth) at various depths on the top of the shoal and equally in the deep regions around the shoal. In the case of our random waves, the large values for BFI and the narrower width of the spectra lead to MI evolution and to a "rogue sea" state, that is, a highly intermittent sea state characterized by a high density of unstable modes (see Figs. 14 and 15). Our results are very similar with the same types of studies reported.[9]

By using the calculations of the spectral bandwidths for all our experimental time series at different locations and for the three types of significant wave heights (steepness), we can correlate these data with the mean wave height. The result is presented in Fig. 16. We note the formation of two separate clusters of higher positive correlation: one for small waves with a large spectral bandwidth and the other localized for the breather/soliton/RW events described by large wave heights and narrower spectra.

Another statistical feature that can confirm the formation of coherent traveling packages of breather/soliton types (KM, Peregrine, and AB solutions) is the distribution of the probability for the wave heights, which we present in Fig. 17. The middle frame, representing regions with coherent package formation, shows evidence of a cluster of narrow bandwidth spectra associated with

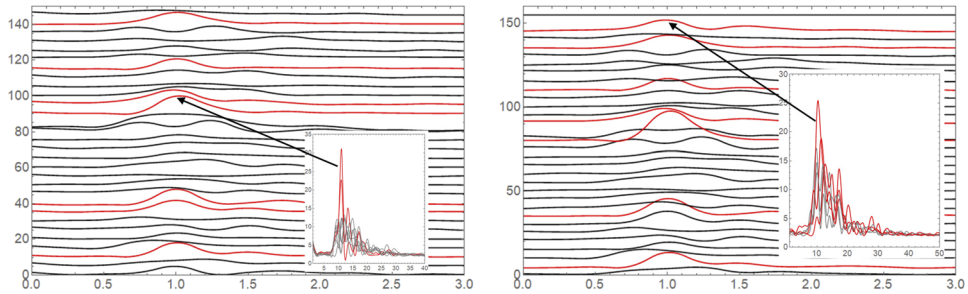

FIG. 13. Same type of spectral representation as in Fig. 12 for H_s = 5.2 cm (left frame) and H_s = 6.2 cm (right frames) for gauge 3 (9 m). In addition, we present in the insets the details of the Fourier spectrum of nine wave series centered at the moment of time indicated by the arrow: the red spectra are associated with coherent packages identified as breathers/solitons, and the gray spectra are the random background waves at nearby points and neighbor moments. The horizontal scale of the insets is in 10× s, and the highest red peak is centered at 1.16 s. Combined relative errors from wave profile measurements and numerical evaluation do not exceed 5%.

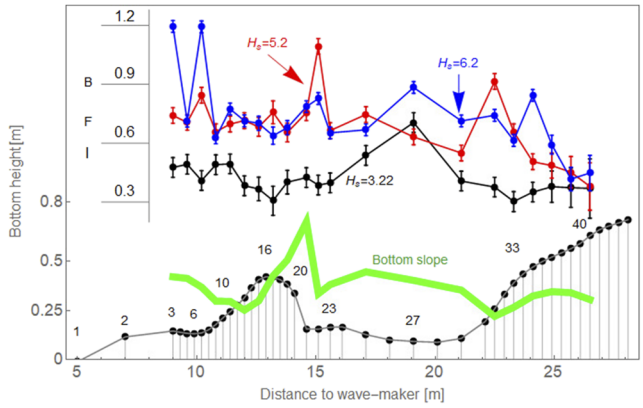

FIG. 14. Plot of the average BFI values over 16 s duration vs space along the wave tank. Legend: H_s = 3.22 cm (black curve), H_s = 5.2 cm (red curve), and H_s = 6.2 cm (blue curve) for the upper curves. The bottom profile and some gauge numbers are represented by the lowest gray curve, and the slope of the water depth (dh/dx) is represented by the green curve. The MI threshold kh = 1.363 happens around gauges 33–34 at $x \simeq 24$ m from the wave maker.

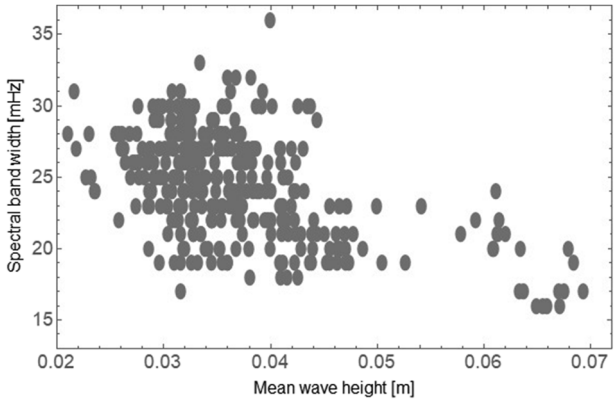

FIG. 16. Correlation between the spectral bandwidth (vertical axis in mHz) and the mean wave height (in meters) measured at each gauge from 1 to 22 for all H_s. The points represent a set of 15 mean values of wave spectra, and wave heights are evaluated across 150 s time series in samples of 10 s each for 22 gauges. The two resulting clusters describe random waves (low wave heights and higher frequencies) and breathers (higher waves and lower frequencies). The semi-axes of the ellipsoidal markers represent the error bars.

these breathers. In Fig. 18, we present the wave height probability distributions for different moments of time over 5 m length. We observe the formation of three main modes: a dominant low-amplitude mode, a dominant high-amplitude mode, and a flat probability distribution, which occasionally tends to shift into a bi-modal unstable mode as predicted by the Soares model.[32]

Our experimental results, mainly gathered in Figs. 9, 10, 12–15, 17, and 18, are in good agreement with the numerical calculation obtained by Trulsen *et al.*[36] from the Boussinesq model with improved linear dispersion and with the experiments presented by Trulsen *et al.*[36] Indeed, a significantly increased BFI value and, consequently, an increase in the probability of RW occur as waves propagate into shallower water. For smaller H_s and $\varepsilon = H_s k_p$, the maximum is smaller and delayed, while for larger steepness, the maximum occurs earlier and is larger (Fig. 14). Increased values of skewness, kurtosis, and BFI are found on the shallower side of a bottom slope, with a maximum close to or slightly after the end of the slope (Figs. 10 and 14). The maxima of the statistical parameters are also observed where the uphill slope is immediately followed by a downhill slope. In the case that waves propagate over a slope from shallower to deeper water, in the theoretical evaluations from Ref. 36, it was not found on an increase in RW wave occurrence where the wave parameters were $ak_p = 0.038$, $a/h = 0.035$, and $Ur = 0.031$. In our experiments, however, we noted this increase in the BFI, kurtosis, and steepness when traveling deeper, probably because our wave parameters, shown in Table II, are different: $ak_p > 0.05$, $a/h = 0.04$, and $U_r > 0.2$.

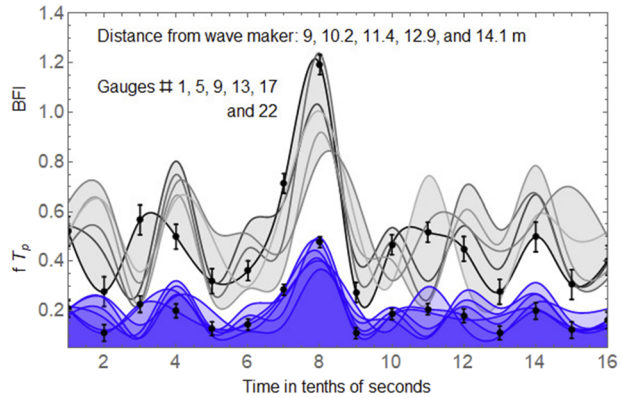

FIG. 15. The gray upper curves represent interpolation of the BFI vs time for six selected gauges. The large central peak of BFI > 1 coincides with the formation of breathers at that position/moment. All five curves show the same reproducible behavior. The blue profiles at the bottom represent the relative value of the peak frequency in the time series recorded at the six selected gauges (1, 5, 9, 13, 17, and 22). Error bars are presented for the BFI of gauge 1 as an example for all results.

IV. COMPARISON WITH EXACT SOLUTIONS

In this section, we present some current theoretical models that can fit our experiments with random waves generated in a L = 50 m long, 2 m wide wave tank with variable bottom and maximum depth h_{max} = 0.76 m presented by the wave maker and at two-thirds of the length (see Figs. 1 and 3). Since in all experiments described in Sec. II we note the formation of stable, traveling coherent wave packages, we present in Sec. IV A the match between these waves and deep-water breathers. All our results put in evidence such traveling localized waves, such as the cases H_s = 5.2 cm and 6.2 cm from Figs. 19 and 20. The denser double traces in these figures are evidence of formation and survival of such localized nonlinear waves, most likely breathers or even higher-order (doublets) breathers, as we will discuss below. We divide this section in two parts: in the first part, we present the corresponding theoretical results for uniform bottom, and in the second part, we extend this case to variable bathymetry.

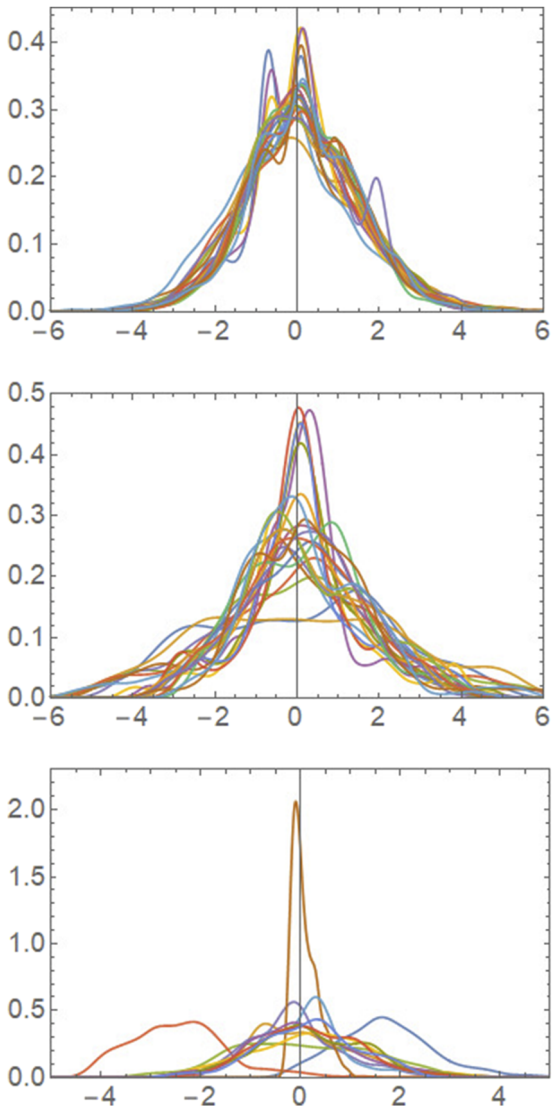

FIG. 17. Probability distributions for the wave heights for H_s = 5.2 cm. Top: mean values calculated across 160 s time series and 10.1 m fetch for gauges 1–22. Center: mean values calculated for the interval 30 s–36 s and 5 m fetch for gauges 1–22. We note the cluster of narrow bandwidth spectra associated with the breathers present within this time interval and location. Bottom: mean values for the interval 88 s–98 s and 7 m fetch for gauges 30–46 at 22 m–29 m from the wave maker. This spectrum contains mainly unstable structures resembling peakons and breaking waves.

In the uniform bottom case, for an ideal (incompressible and inviscid) liquid under the hypothesis of irrotational flow, the dynamics of a free surface flow is described by the Laplace equation for the velocity potential and two boundary conditions: a nonlinear one (kinetic) on the free surface and a zero vertical velocity component at the rigid bottom.[1,11] Under the assumption of very small amplitude waves (or steepness), the problem can be considered a weakly nonlinear one, and the standard way of modeling is to derive the NLS equation by expanding the surface elevation and the velocity potential in power series and using the multiple scale method.[1,2,11,12,46]

The procedure is to introduce slow independent variables (both for time and space) and treat each of them as independent. The extra degrees of freedom arising from such variables allow one to remove the secular terms that may appear in the standard expansion. The multiple scale expansion is usually performed in physical space, and a simplification of the procedure is the requirement that the waves are quasi-monochromatic. In the approximation of infinite water depth, for two-dimensional waves, the surface elevation, up to third order in nonlinearity, takes the form

$$\eta(x,t) = \left(|A(x,t)| - \frac{1}{8}k_p^2|A(x,t)|^3\right)\cos\theta + \frac{1}{2}k_p|A(x,t)|^2\cos(2\theta) + \frac{3}{8}k_p^2|A(x,t)|^3\cos(3\theta) + \cdots, \tag{7}$$

where $A(x, t)$ is a complex wave envelope, k_p is the wave number of the carrier wave, $\eta(x, t)$ is the water elevation, $\theta = (k_p x - \Omega_0 t + \phi)$ is the phase, and ϕ is a constant phase. In addition, we know that $\Omega_0 = \omega_p(1+k_p^2|A(x,t)|^2/2)$ is the nonlinear dispersion relation, with $\omega_p = \sqrt{gk_p}$. The complex envelope obeys the NLS equation

$$i\left(\frac{\partial A}{\partial t} + c_g\frac{\partial A}{\partial x}\right) - \frac{\omega_p}{8k_p^2}\frac{\partial^2 A}{\partial x^2} - \frac{1}{2}\omega_p k_p^2|A|^2A = 0, \tag{8}$$

with $c_g = \partial\omega/\partial k$ being the group velocity. The NLS equation (8) has various types of traveling solutions known as breathers or solitons. One analytic solution with major impact in the literature is a combined one-parameter α family given by[2]

$$A(X,T) = A_0 e^{2iT}\left(1 + \frac{2(1-2\alpha)\cosh(2RT) + iR\sinh(2RT)}{\sqrt{2\alpha}\cos(\Omega X) - \cosh(2RT)}\right), \tag{9}$$

where X, T are arbitrary variables scaled by a factor s and the solution $A(x, t) = sA(sX, s^2T)$, $R = \sqrt{8\alpha(1-2\alpha)}$, and $\Omega = 2\sqrt{1-2\alpha}$. When the parameter $\alpha \in (0, 0.5)$, Eq. (9) describes the space-periodic Akhmediev Breather (AB) family, and when $\alpha > 0.5$, Eq. (9) describes the time-periodic Kuznetsov–Ma (KM) soliton.[2,11] Moreover, in the singular value for the parameter $\alpha = 0.5$, Eq. (9) describes a rational solution known as the Peregrine (P) solution,[26]

$$A(X,T) = A_0 e^{2iT}\left(-1 + \frac{4 + 16iT}{1 + 4X^2 + 16T^2}\right). \tag{10}$$

The Peregrine solution in Eq. (10) only represents the lowest-order solution of a family of doubly localized Akhmediev–Peregrine (AP) breathers,[16,28] also called higher-order breathers,[2]

$$A_j(X,T) = e^{2iT}\left((-1)^j + \frac{G_j + iH_j}{D_j}\right), \tag{11}$$

where the terms G_j, H_j, D_j are polynomials, which can be generated by a recursion procedure.[16]

A. Non-uniform bathymetry

While in deeper water, third-order nonlinearity causes focusing of long-crested and narrow-banded waves and hence possibility of occurrence of freak waves, in shallower water, the nonlinear

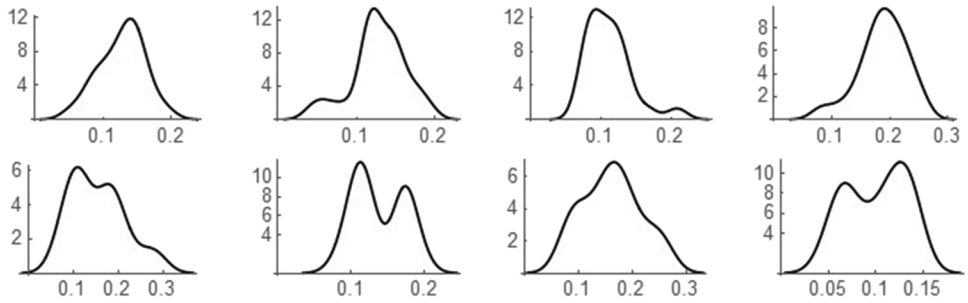

FIG. 18. Wave height probability distributions for different moments of time, from upper left corner CW: t = 1 s, 2 s, 15 s, 20 s, 35 s, 50 s, 60 s, and 75 s. Each distribution calculated over 2 s interval (100 samples) over the fetch 9 m–14 m (gauges 3–22) for H_s = 5.2 cm. Three main modes are present: dominant low-amplitude waves at t = 15 s and 35 s, dominant high-amplitude waves at t = 1 s, 2 s, 20 s, and 60 s, and flat PDF distribution at t = 35 s. Occasionally, the distribution becomes bi-modal. We also note a cyclic behavior since certain types of PDF tend to repeat.

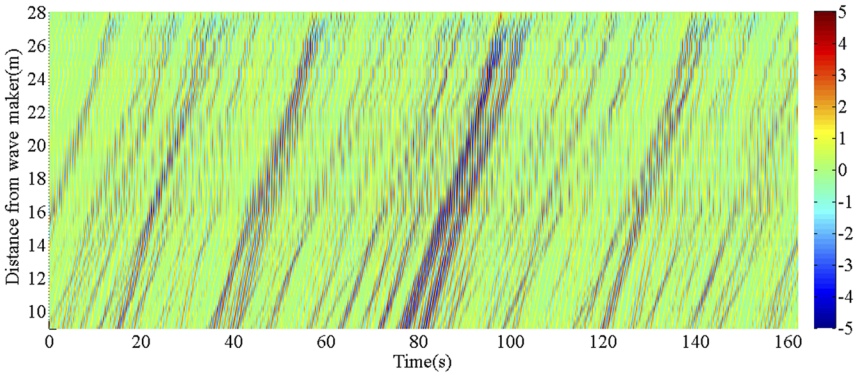

FIG. 19. Density plot of the space–time wave field for H_s = 5.2 cm waves (wave amplitude scale in cm to the right). The gauges from 3–20 with 30 cm separation, the gauges from 20–24 with 50 cm separation, the gauges from 24–30 with 100 cm separation, and the gauges from 30–33 with 40 cm separation. Higher-order breathers (doublets) can be observed by their red-blue color while propagating uniformly.

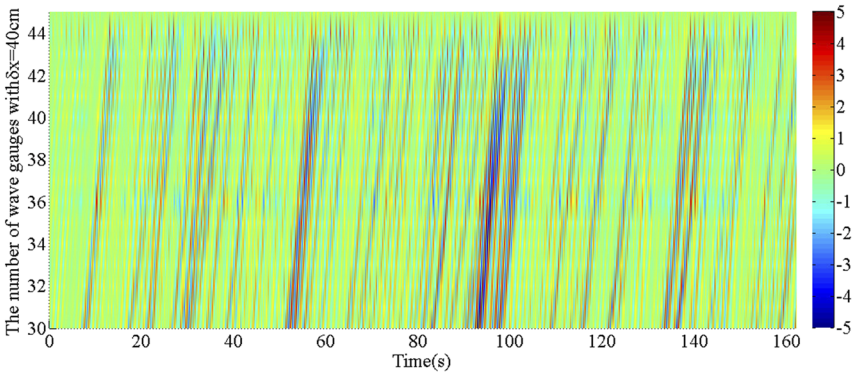

FIG. 20. Density plot of the space–time wave field for the H_s = 6.2 cm waves. Legend for wave amplitude in cm to the right.

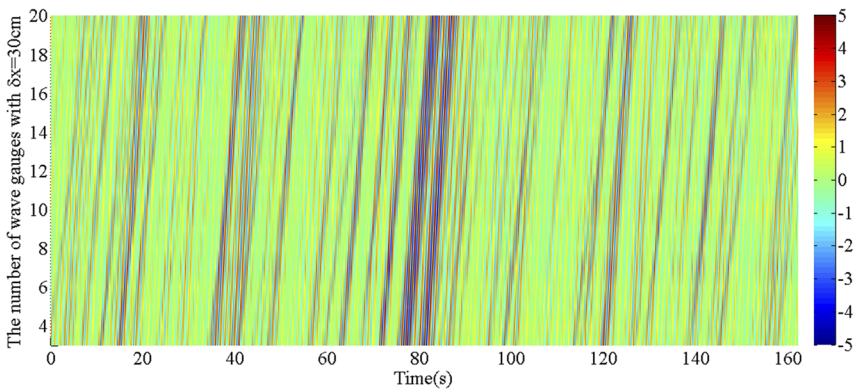

dynamics are dominated by second-order nonlinearity. Waves over variable water depth can be modeled for irrotational, inviscid, and incompressible flow with a variable coefficient NLS equation.[13,46] In the approximation of finite depth $(kh)^{-1} = \mathcal{O}(1)$, mild slope $\partial h/\partial x = \mathcal{O}(2)$, and small steepness $\varepsilon = \mathcal{O}(3)$, the authors of Ref. 42 presented a NLS model with variable coefficients plus a shoaling term. In this model, water surface displacement η [Eq. (7)] and velocity potential Φ can be written as third-order perturbation series normalized to g and ω_p, respectively,

$$\eta = \varepsilon^2\bar{\eta} + \frac{1}{2}(\varepsilon A e^{i\theta} + \varepsilon^2 A_2 e^{2i\theta} + \cdots + \text{c.c.}), \tag{12}$$

$$\Phi = \varepsilon\bar{\phi} + \frac{1}{2}(\varepsilon A_1' e^{i\theta} + \varepsilon^2 A_2' e^{2i\theta} + \cdots + \text{c.c.}), \tag{13}$$

where $\varepsilon\theta = \int^x k(\xi)d\xi - t$ and c.c. means complex conjugation. The resulting NLS modified [with respect to Eq. (8)] equation in terms of the first harmonic amplitude A of the surface displacement is

$$i\mu\frac{dh}{dx}A + i\left(\frac{\partial A}{\partial x} + \frac{1}{v_g}\frac{\partial A}{\partial t}\right) + \lambda\frac{\partial^2 A}{\partial t^2} = \nu|A|^2 A, \tag{14}$$

where the coefficients $\mu, \lambda, \nu, \bar{\omega}$ depending on k, h, and v_g at constant imposed ω are defined in Ref. 42. In particular, the extra shoaling term $i\mu h_x$ generalizing the traditional NLS equation (8) comes from the conservation of wave action flux.[39] For the specific bathymetry in our experiments (Figs. 1–3), when the waves travel over the shoal (at $x \sim 11$–15 m from the wave maker), the dispersion coefficient $\lambda(h)$ has only a slow variation of maximum 12% of its value. The nonlinear term coefficient $\nu(h)$ decreases on top of the shoal with 54% of its deep-water value, while the shoaling term coefficient $\mu(h)$ has a local increase of 140% on top of the island. The effect of the shoaling term, similar mathematically to the linear dissipative terms occurring in a non-homogeneous medium or to the boundary-layer induced dissipation term in uniform depth, is a change in wave's amplitude. Actually, it was found[46] that such damping terms can stabilize the BF instabilities, especially since the nonlinear term contribution decreases in the shoaling regions. This effect is visible in our experiments, manifesting as a decrease in the BFI over the shallower region for any H_s value (Fig. 14). Analyzing Eq. (14) with the Djorddjevićć–Redekopp model[46] results in

$$\frac{dh}{dx} \sim -\frac{dk_p}{dx} \sim \frac{d|A|}{dx}, \tag{15}$$

where these relationships are in effect because the shoaling term coefficient can be absorbed in the relation $\mu \sim dv_g/dx$. Equation (15) implies that waves entering a shallower region experience a decreasing amplitude and wavelength, while waves expanding over deeper regions experience amplitude and wavelength growth. This effect is clearly visible in our results; see, for example, Figs. 3–6 and 8. Such effects, including the enhancement of the RW probability of formation, were also predicted by using an exact Hamiltonian formalism, inducing a fully nonlinear refocusing of transient wave groups traveling over a sloping bottom of finite depth.[50]

In the following, we return to Figs. 14 and 15 for the BFI space–time distribution for the three different wave steepness. Where the water depth is larger (gauges 3–8 and 21–28), BFI has larger values,

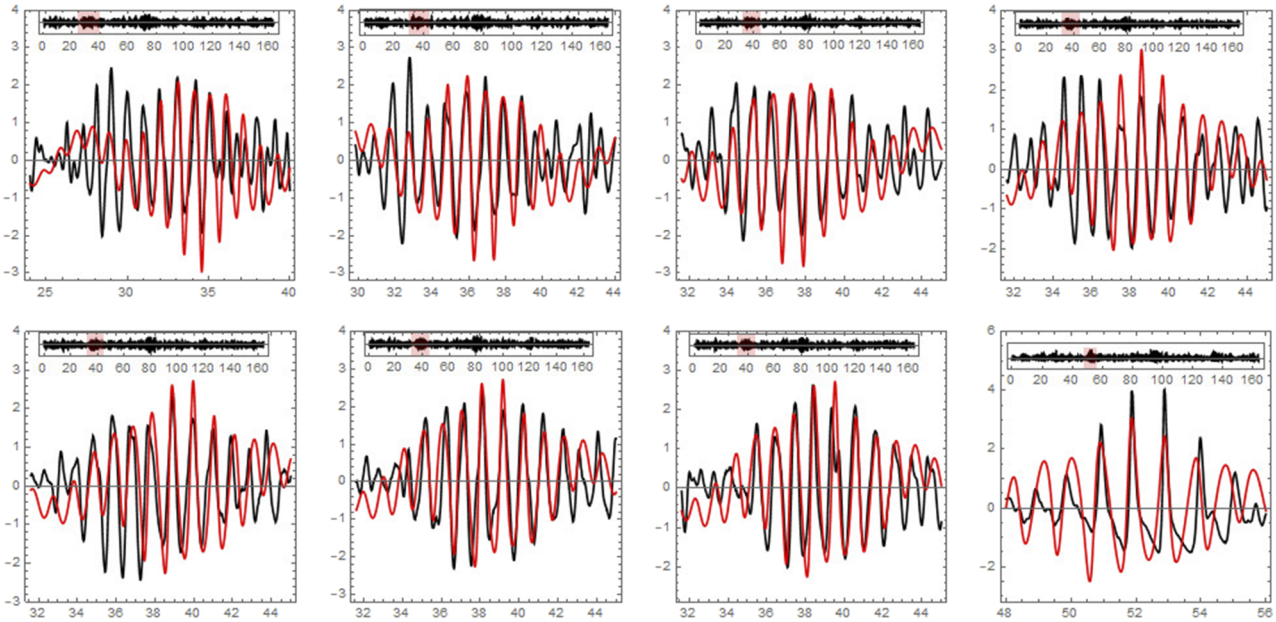

FIG. 21. Black curves in the main frames are the experimental wave profiles for H_s = 3.22 cm, measured at gauges 3, 13, 20, 21, 22, 23, 24, 26, 44 (from upper left corner clockwise), thus covering a fetch of 21 m beginning at 9 m from the wave maker. The time interval is shown in the upper inset highlighted in red. Red curves are theoretical KM breather solutions of the NLS equation for deep water. The only parameters changing from one frame to another are the origin time, while the rest of the KM breather parameters (A_0, α) are the same for all frames, the fact that validates the correctness of our model.

and this value increases with the steepness as we can see from the red and blue curve spikes at gauges 7, 22, and 27. For example, this effect is quite visible over gauges 23–28 where BFI increases monotonically with water depth and again over gauges 27–30 where BFI decreases monotonically with the decrease in the water depth. Over regions with shallower water depth (kh is closer to the MI threshold), the BFI decreases irrespective of the steepness (see black, red, and blue curves over gauges 11–20 in Fig. 14). However, the dynamic response of the waves depends on a combination of water depth (gray curve with circles), bottom slope (green thick curve), and wave steepness (in order of its increasing upper curves: black, red, blue). At a sudden drop in the water depth, higher steepness tends to reveal a higher BFI; hence, steeper waves are more likely to build RW after shoals and islands (gauge 21).

Over regions where water becomes permanently shallower (gauges 30–40), the relaxation distance for decreasing and stabilizing the BFI, kurtosis, and skewness depends on the wave steepness. While at H_s = 3.22 cm, the BFI variation is almost monotonically correlated with the water depth variation, for larger waves with H_s = 5.2 cm–6.2 cm, the BFI spikes back to larger values and is not stabilized for a length of about 8 m–10 m $\gg \lambda_p$, as mentioned in Ref. 42.

We also noted that for small values of the bottom slope in absolute values on the shallow side of the slope, kurtosis and skewness can stabilize almost at the same location as the change in depth. Large local values of the absolute value of the bottom slope (such as fast drops or steep increases of the bottom represented by the spikes of the green curve in Fig. 14 over gauges 20–21 or 31–32) induce spikes in the BFI, and this effect is stronger for larger wave steepness and less prominent for smoother waves such as in the case of H_s = 3.22 cm. This effect can be correlated with the observation of similar spikes in kurtosis and skewness at the same locations (Fig. 10), and these observations are in agreement with the experiments in Ref. 36 and numerical evaluations in Ref. 38. The increase in skewness and kurtosis over shallowing regions, especially in the transition zone, was also correlated with deviations of the wave states from the Gaussian distribution and the increase in the probability of RW occurrence. These changes in the statistical parameters of the wave field over the transition zone depend on the wave steepness (and, consequently, on the Ursell number and H_s), but not necessarily on the length of the transitional zone, as we noted the occurrence of localized spikes at the beginning of any high bottom slope region that do not necessarily continue along the shallower region. The results

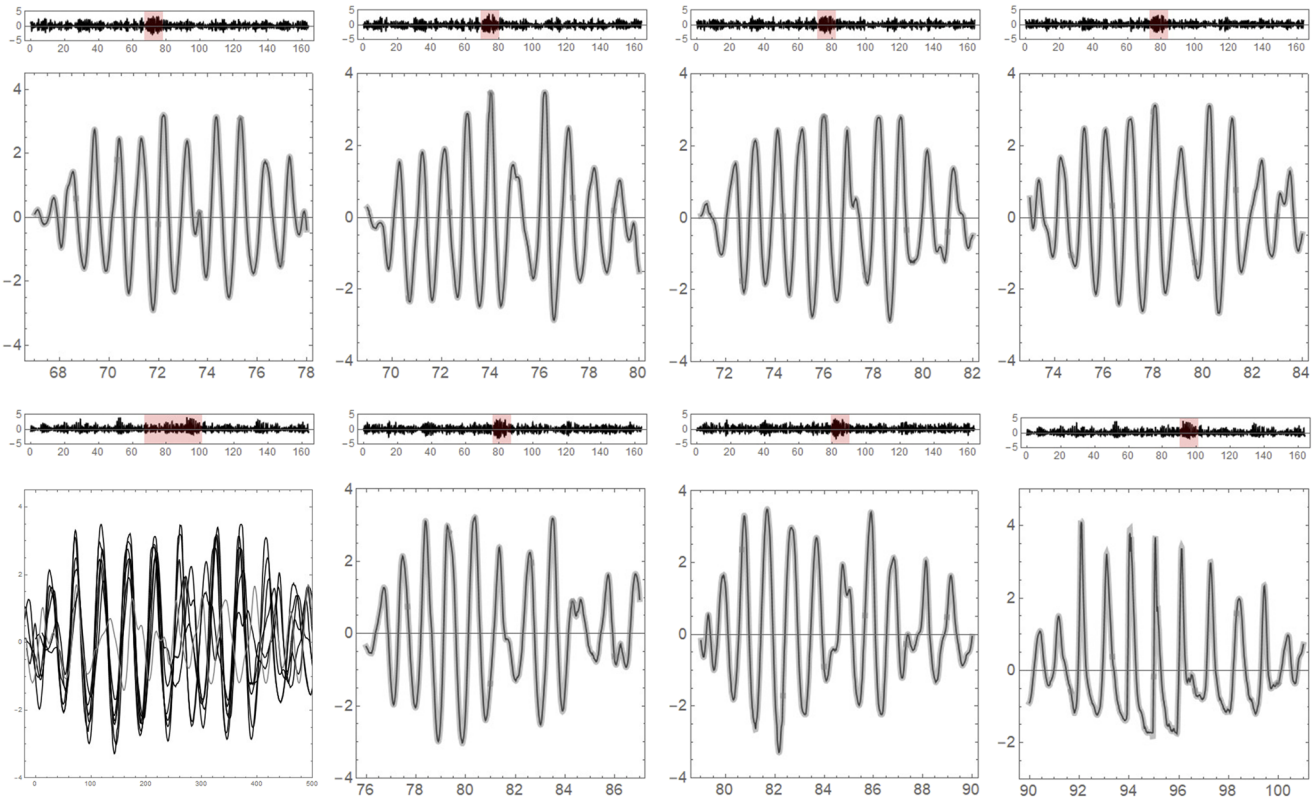

FIG. 22. From upper left CW: black curves in the first seven frames are experimental wave profiles measured at gauges 3, 12, 19, 20, 21, 22, 23, 25, 43, thus covering a fetch of 21 m beginning at 9 m from the wave maker. The gray stripes are error bars around mean values. The time interval is shown in the upper inset highlighted in red. The last frame represents an overlap of all seven frames, shifted in time correspondingly. The final frame shows a clear match of the same type of behavior for this coherent traveling group and the likeliness to be described as a breather, possibly a higher-order breather.

obtained confirm the conclusion made[13,35,36] in the framework of the nonlinear Schrodinger equation for a narrow-banded wind wave field that the kurtosis and the number of freak waves may significantly differ from the values expected for a flat bottom of a given depth.

While the wave propagates over the uphill slope from deeper to shallower water, it becomes evidence from Figs. 10 and 14 that as long as the shallower side of the slope is sufficiently shallow and the slope length is small enough, we observe local maxima (spikes) of kurtosis, skewness, and BFI. These localized maxima are placed at the shallower end of the slopes in agreement with the results from Ref. 36. In our experiments, the bottom mimics a realistic ocean floor, and the regions with almost constant water depth are not very long, so we do not observe the asymptotic stabilization of kurtosis and skewness.

B. Exact solution match for experiments

We fit the traveling coherent wave packages obtained in our experiments; see, for example, the red stripes in Figs. 4–6 or the wave packages easily visible in Figs. 7 and 8, with all the above solutions trying to identify which one best describes our results.

In Fig. 21, we fit the earliest coherent package formed in small steepness waves with KM solitons. In the experiment, this group travels as a doublet of stable localized waves, and it is not obvious whether this is a bound group of two independent KM solitons or it is one AB double-breather (higher-order Peregrine breather). All theoretical breathers presented in Fig. 21 have the same set of parameters, except being translated in space and time according to the gauge position and chosen interval of time. It is very interesting that the match keeps being good enough while the group travels over variable bottom, over a shoal, and the deep valley following, and even up the beach when the waves increase in amplitude and become pretty sharp (see the eighth frame, for example) and ready to break.

In Fig. 22, we do not show the theory but instead present an overlap of seven instants of the same wave group, shifted in time correspondingly. The eighth frame shows an obvious match of the same type of behavior for this coherent traveling group and the likeliness to a breather, possibly a higher-order breather

We also present the match of the stable traveling doublet with two KM solitons bound together [Fig. 23 (left)] as compared to a best fit with a single KM soliton, presented in the right frame. In Fig. 24, we fit the experiment with Peregrine breathers (red curves) and solitons, and for comparison, the same experimental instants were fitted with KM solitons (blue curves). In Figs. 25 and 26, we present comparison with double AB breathers [Eq. (11)]. This modeling represents the best match, so we believe that the stable, oscillating, and traveling doublets are actually higher-order AB submerged in a random wave background. There is also a possibility to explain these oscillating and breathing doublets as Satsuma–Yajima solitons and the supercontinuum generation effect.[2,11]

The same qualitative results and the same percentage of matching are obtained for the other two experiments of higher steepness, but we do not present them here in detail, in order to keep a reasonable length for this paper. In Figs. 19 and 20, we present density plots of the wave heights, in space–time frames, for the steeper waves. These plots show constant group velocity traveling breathers over the shoal and deep valleys.

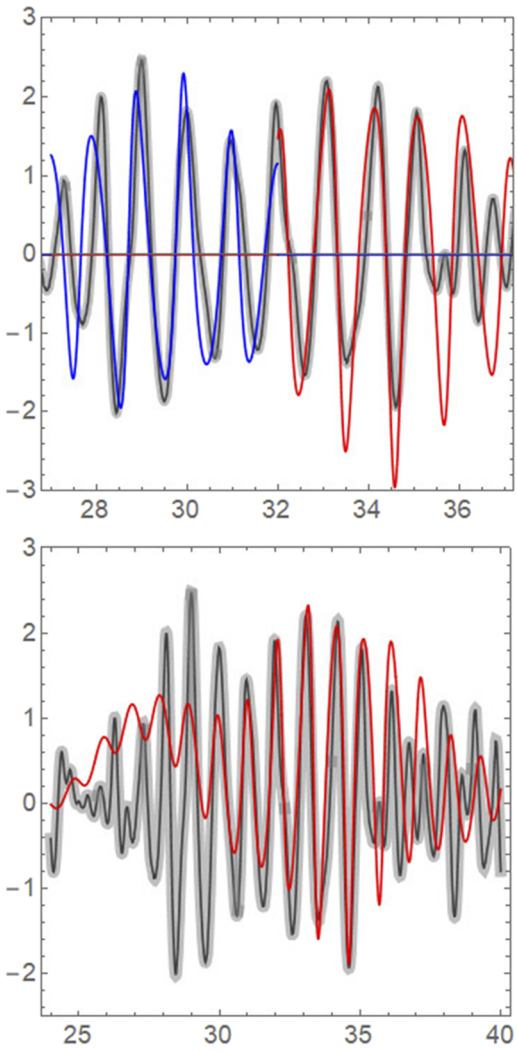

FIG. 23. Matching H_s = 3.22 cm waves, experimental data, and error represented by gray stripes. Top: gauge 3 at t = 28 –37 s matched with two KM solitons (blue and red). Bottom: gauge 13 at t = 30 s–44 s matched with one KM soliton (red).

In our experiments, the mean value of steepness is 0.0765 ± 4%, and the theoretical one obtained from the match of experiments with the same KM or Peregrine breather results in 0.078 03, showing a good match between experiments and theory. The match was made between the analytic form of the KM breather and the experiment for gauges 4, 10, 12, 18, 19, 20, 23, 25, 28, 30, and 34. Since ocean waves are usually characterized by an average steepness of about $\varepsilon \sim 0.1$ corresponding to the peak frequency of the spectrum, both the experimental and theoretical match are plausible. From measurement of the time interval when this structure arrives at various gauges, we obtain a group velocity for the breather of $V_g = 0.81$ m/s. The theory predicts the occurrence of maximum heights of these breathers in the range $A_{max}/A_0 \sim 3.92$, which is in good agreement with our experimental values of 3.41.

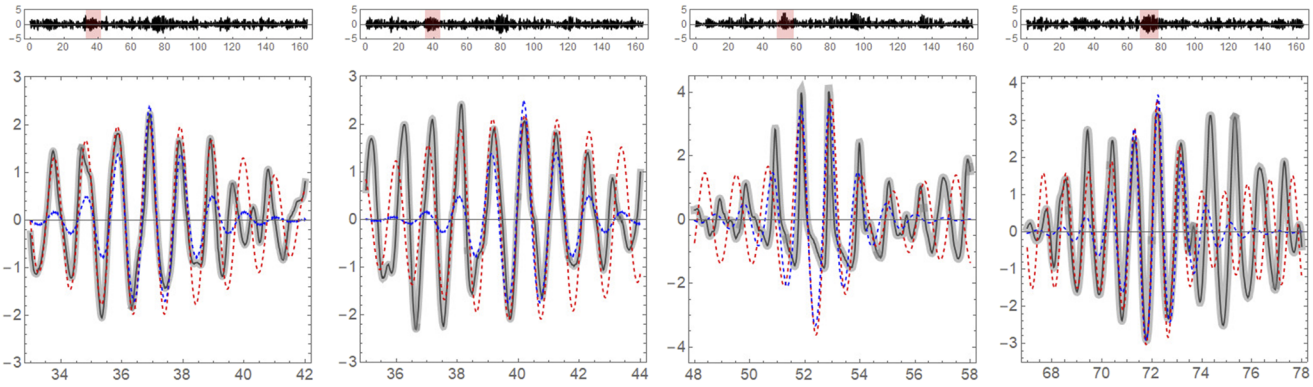

FIG. 24. H_s = 3.22 cm waves. The thick gray bands centered on black experimental curves are the error bars, red curves are Peregrine solitons, and blue curves are KM solitons. From left, first three frames represent matching an earlier formed coherent package: gauge 13 at t = 34 s–42 s, gauge 23 at t = 36 s–44 s, and gauge 44 at t = 48 s–58 s. Gauge 3 at t = 68 s–78 s matching a later formed coherent package.

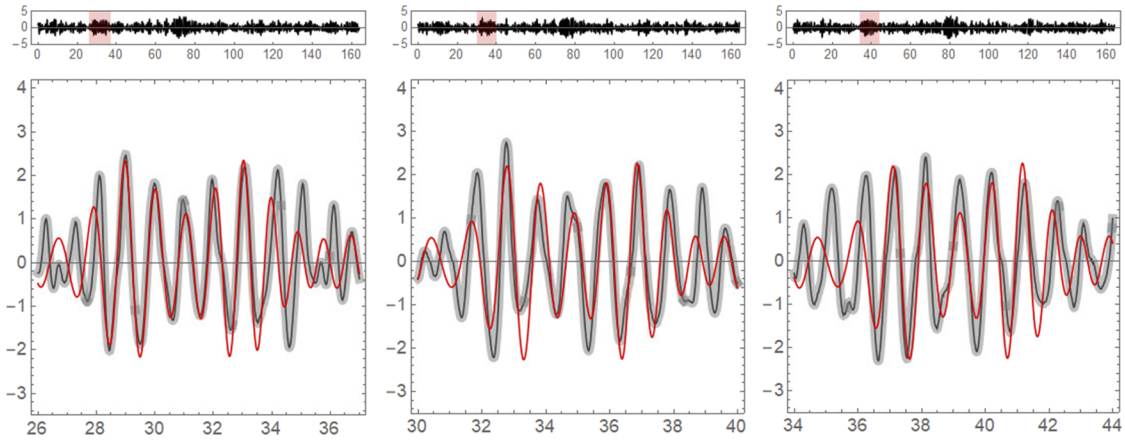

FIG. 25. H_s = 3.22 cm experimental waves plotted with thick gray error bands and central black curves with their theoretical match (red curves) with double AB breathers. From left: gauge 3 at t = 26 s–36 s, gauge 13 at t = 30 s–40 s, and gauge 23 at t = 34 s–44 s.

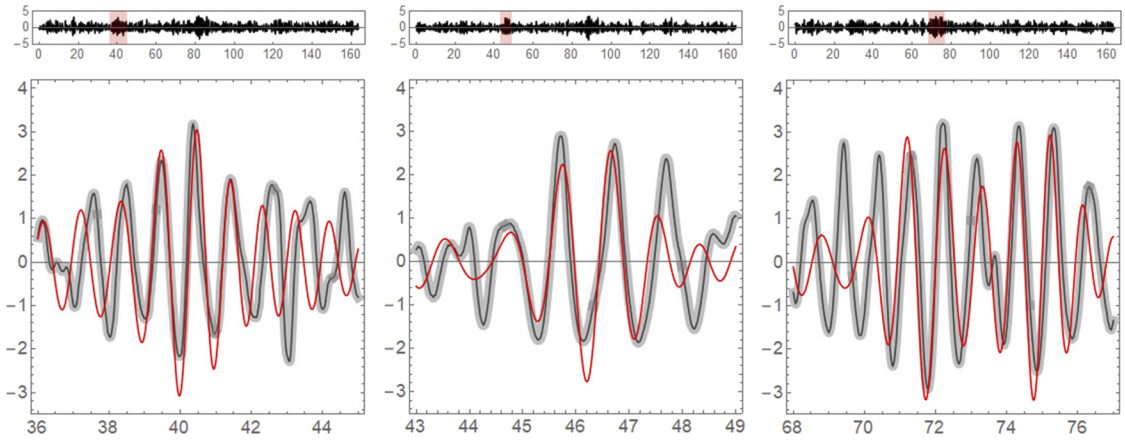

FIG. 26. H_s = 3.22 cm experimental waves plotted with thick gray error bands and central black curves with their theoretical match (red curves) with double AB breathers. From left: gauge 26 at t = 26 s–46 s, gauge 31 at t = 43 s–49 s, and again gauge 3, the latest coherent group at t = 68 s–77 s.

V. CONCLUSIONS

In this paper, we present experimental results describing the dynamics of a random background of deep uni-directional, long-crested, water waves over non-uniform bathymetry consisting in a shoal and several deeper valleys, as well as a final run-up beach. Experiments were performed with waves initially generated with a JONSWAP spectrum, keeping the same carrier (central) frequency, but for three different wave significant heights, involving three different wave steepness. The experimental results confirm the formation of very stable, coherent localized wave packages that travel with almost uniform group velocity across the variable manifolds of the bottom. By using well established statistical tools and by matching experiments with some of the exact solutions of the NLS equation, we proved that these coherent wave packages coming out of the random background are actually deep-water breather/soliton solutions (mainly Kuznetsov–Ma, Akhmediev, higher-order AB, and Peregrine breather/soliton types), and we put into evidence the formation of rogue waves around those regions where the BFI, kurtosis, and skewness predict their formation by taking larger values. The evolution and distribution of the statistical parameters, i.e., space and time variation of kurtosis, skewness, and BFI, Fourier and moving Fourier spectra, and probability distribution of wave heights, are interpreted in terms of the balance of the terms in a generalized NLS equation for non-uniform bathymetry, having variable coefficients and a shoaling extra term.

ACKNOWLEDGMENTS

Parts of this work were supported by the Natural Science Foundation of China under Grant Nos. NSFC-51639003 and NSFC-51679037. A.L. is grateful to Dalian University of Technology for hospitality during the accomplishment of this research project in 2018–2019. The present work was also supported by the National Key Research and Development Program of China (Grant Nos. 2019 YFC0312400 and 2017 YFE0132000), the National Natural Science Foundation of China (Grant Nos. 51975032 and 51939003), and the State Key Laboratory of Structural Analysis for Industrial Equipment (Grant No. S18408).

DATA AVAILABILITY

The data that support the findings of this study are available from the corresponding author upon reasonable request.

REFERENCES

[1]Z. Hu, W. Tang, H. Xue, and X. Zhang, "Numerical study of rogue waves as nonlinear Schrödinger breather solutions under finite water depth," Wave Motion **52**, 81–90 (2015).
[2]*Rogue and Shock Waves in Nonlinear Dispersive Media*, edited by M. Onorato, S. Residori, and F. Baronio (Springer, Heidelberg, 2016).
[3]X.-B. Wang, T.-T. Zhang, and M.-J. Dong, "Dynamics of the breathers and rogue waves in the higher-order nonlinear Schrödinger equation," Appl. Math. Lett. **86**, 298–304 (2018).
[4]L. Fernandez, M. Onorato, J. Monbaliu, and A. Toffoli, "Occurrence of extreme waves in finite water depth," in *Extreme Ocean Waves*, edited by E. Pelinovsky and C. Kharif (Springer, Cham, Switzerland, 2015), pp. 45–62.
[5]J. M. Dudley, F. Dias, M. Erkintalo, and G. Genty, "Instabilities, breathers and rogue waves in optics," Nat. Photonics **8**, 755 (2014).
[6]F. Baronio, M. Conforti, A. Degasperis, S. Lombardo, M. Onorato, and S. Wabnitz, "Vector rogue waves and baseband modulation instability in the defocusing regime," Phys. Rev. Lett. **113**, 034101 (2014).
[7]I. Shugan, S. Kuznetsov, Y. Saprykina, and Y. Y. Chen, "Late stages in the development of modulation instability of waves," in *ASME 2018 37th International Conference on Ocean, Offshore and Arctic Engineering* (The American Society of Mechanical Engineers, Madrid, 2018).
[8]B. F. Akers, "Modulational instabilities of periodic traveling waves in deep water," Physica D **300**, 26–33 (2015).
[9]C. F. Wu, R. H. J. Grimshaw, K. W. Chow, and H. N. Chan, "A coupled "AB" system: Rogue waves and modulation instabilities," Chaos **25**, 103113 (2015).
[10]J. Wang, Q. W. Ma, S. Yan, and A. Chabchoub, "Breather rogue waves in random seas," Phys. Rev. Appl. **9**, 014016 (2018).
[11]A. Chabchoub, M. Onorato, and N. Akhmediev, "Hydrodynamic envelope solitons and breathers," in *Rogue and Shock Waves in Nonlinear Dispersive Media*, LNP Vol. 926, edited by M. Onorato, S. Residori, and F. Baronio (Springer, Heidelberg, 2016), pp. 55–88.
[12]A. I. Dyachenko, D. I. Kachulin, and V. E. Zakharov, "Super compact equation for water waves," J. Fluid Mech. **828**, 661–679 (2017).
[13]H. D. Zhang, C. G. Soares, M. Onorato, and A. Toffoli, "Modelling of the temporal and spatial evolutions of weakly nonlinear random directional waves with the modified nonlinear Schrödinger equations," Appl. Ocean Res. **55**, 130–140 (2016).
[14]W. Choi, "On Rayleigh expansion for nonlinear long water waves," J. Hydrodyn. **31**, 1115–1126 (2019).
[15]V. Zakharov and A. Gelash, "Nonlinear stage of modulation instability," Phys. Rev. Lett. **111**, 054101 (2013).
[16]S. A. Chin, O. A. Ashour, S. N. Nikolić, and M. R. Belić, "Maximal intensity higher-order Akhmediev breathers of the nonlinear Schrödinger equation and their systematic generation," Phys. Lett. A **380**, 3625–3629 (2016).
[17]D. Kachulin, A. Dyachenko, and V. Zakharov, "Soliton turbulence in approximate and exact models for deep water waves," Fluids **5**, 67 (2020).
[18]A. Chabchoub, B. Kibler, C. Finot, G. Millot, M. Onorato, J. M. Dudley, and A. V. Babanin, "The nonlinear Schrödinger equation and the propagation of weakly nonlinear waves in optical fibers and on the water surface," Ann. Phys. **361**, 490–500 (2015).
[19]J. Chen and D. E. Pelinovsky, "Rogue periodic waves of the focusing nonlinear Schrödinger equation," Proc. R. Soc. A **474**, 20170814 (2018).
[20]A. Chabchoub and R. H. J. Grimshaw, "The hydrodynamic nonlinear Schrödinger equation: Space and time," Fluids **1**, 23 (2016).
[21]M. Onorato and P. Suret, "Twenty years of progresses in oceanic rogue waves: The role played by weakly nonlinear models," Nat. Hazards **84**, 541–548 (2016).
[22]A. Goullet and W. Choi, "A numerical and experimental study on the nonlinear evolution of long-crested irregular waves," Phys. Fluids **23**, 016601 (2011).
[23]T. A. A. Adcock and P. H. Taylor, "Non-linear evolution of uni-directional focussed wave-groups on a deep water: A comparison of models," Appl. Ocean Res. **59**, 147–152 (2016).
[24]B. Kibler, A. Chabchoub, A. Gelash, N. Akhmediev, and V. E. Zakharov, "Superregular breathers in optics and hydrodynamics: Omnipresent modulation instability beyond simple periodicity," Phys. Rev. X **5**, 041026 (2015).
[25]A. Chabchoub, M. Onorato, and N. Akhmediev, "Evolution of extreme wave statistics in surface elevation and velocity field over a non-uniform depth," in *Rogue and Shock Waves in Nonlinear Dispersive Media*, edited by M. Onorato, S. Resitori, and F. Baronio (Springer, Cham, 2016).
[26]G. Dong, B. Liao, Y. Ma, and M. Perlin, "Experimental investigation of the peregrine breather of gravity waves on finite water depth," Phys. Rev. Fluids **3**, 064801 (2018).
[27]L. C. Zhao, L. Ling, and Z. Y. Yang, "Mechanism of Kuznetsov-Ma breathers," Phys. Rev. E **97**, 022218 (2018).
[28]A. Chabchoub, T. Waseda, B. Kibler, and N. Akhmediev, "Experiments on higher-order and degenerate Akhmediev breather-type rogue water waves," J. Ocean Eng. Mar. Energy **3**, 385–394 (2017).

[29]O. Gramstad, E. Bitner-Gregersen, K. Trulsen, and J. C. N. Borge, "Modulational instability and rogue waves in crossing sea states," J. Phys. Oceanogr. **48**, 1317–1331 (2018).
[30]J. M. Dudley, G. Genty, A. Mussot, A. Chabchoub, and F. Dias, "Rogue waves and analogies in optics and oceanography," Nat. Rev. Phys. **1**, 675–689 (2019).
[31]L. Dostal, M. Hollm, and E. Kreuzer, "Study on the behavior of weakly nonlinear water waves in the presence of random wind forcing," Nonlinear Dyn. **99**, 2319–2338 (2020).
[32]S. Støle-Hentschel, K. Trulsen, J. C. N. Borge, and S. Olluri, "Extreme wave statistics in combined and partitioned windsea and swell," Water Waves **2**, 169–184 (2020).
[33]J. M. Soto-Crespo, N. Devine, and N. Akhmediev, "Integrable turbulence and rogue waves: Breathers or solitons?," Phys. Rev. Lett. **116**, 103901 (2016).
[34]A. Chabchoub, "Tracking breather dynamics in irregular sea state conditions," Phys. Rev. Lett. **117**, 144103 (2016).
[35]M. Tian, A. Sheremet, J. M. Kaihatu, and G. Ma, "On the shoaling of solitary waves in the presence of short random waves," J. Phys. Oceanogr. **45**, 792–806 (2015).
[36]K. Trulsen, A. Raustøl, S. Jorde, and L. B. Rye, "Extreme wave statistics of long-crested irregular waves over a shoal," J. Fluid Mech. **882**, R2 (2020). K. Trulsen and S. Jorde, "Extreme wave statistics in the surface elevation and the velocity field for waves propagating over a shoal," Geophys. Res. Abstr. **21**, 1 (2019).
[37]C. Viotti and F. Dias, "Extreme waves induced by strong depth transitions: Fully nonlinear results," Phys. Fluids **26**, 051705 (2014).
[38]G. Ducrozet and M. Gouin, "Influence of varying bathymetry in rogue wave occurrence within unidirectional and directional sea-states," J. Ocean Eng. Mar. Energy **3**, 309–324 (2017).
[39]N. E. Pizzo and W. K. Melville, "Wave modulation: The geometry, kinematics, and dynamics of surface-wave packets," J. Fluid Mech. **803**, 292–312 (2016). V. M. Hur and M. A. Johnson, "Modulational instability in the Whitham equation for water waves," Stud. Appl. Math. **134**, 120–143 (2014).
[40]W. Xia, Y. Ma, and G. Dong, "Numerical simulation of freak waves in random sea state," Procedia Eng. **116**, 366–372 (2015).
[41]C. Lawrence, K. Trulsen, and O. Gramstad, "Evolution of extreme wave statistics in surface elevation and velocity field over a non-uniform depth," in *EGU2020-6007 EGU General Assembly 2020*, edited by G. R. Abstract (Copernicus Publications, Göttingen, 2020).
[42]J. Thomas and R. Yamada, "An amplitude equation for surface gravity wave-topography interactions," Phys. Rev. Fluids **3**, 124802 (2018).
[43]F. Fedele, J. Brennan, S. P. D. Leön, J. Dudley, and F. Dias, "Real world ocean rogue waves explained without the modulational instability," Sci. Rep. **6**, 27715 (2016).
[44]C. Lucas and C. G. Soares, "On the modelling of swell spectra," Ocean Eng. **108**, 749–759 (2015).
[45]A. Chabchoub, G. Genty, J. M. Dudley, B. Kibler, and T. Waseda, "Experiments on spontaneous modulation instability in hydrodynamics," in *the 27th International Ocean and Polar Engineering Conference* (International Society of Offshore and Polar Engineers, 2017).
[46]A. Slunyaev, "Higher-order nonlinear Schrödinger equations for simulations of surface wavetrains," in *EPSC2016-3305 EGU General Assembly*, edited by G. R. Abstract (Copernicus Publications, Göttingen, 2016), Vol. 18. G. K. Rajan, S. Bayram, and D. M. Henderson, "Periodic envelopes of waves over non-uniform depth," Phys. Fluids **28**, 042106 (2016).
[47]C. T. Bolles, K. Speer, and M. N. Moore, "Anomalous wave statistics induced by abrupt depth change," Phys. Rev. Fluids **4**, 011801(R) (2019).
[48]F. Baronio, S. Chen, P. Grelu, S. Wabnitz, and M. Conforti, "Baseband modulation instability as the origin of rogue waves," Phys. Rev. A **91**, 033804 (2015).
[49]K. Trulsen, "Rogue waves in the ocean, the role of modulational instability, and abrupt changes of environmental conditions that can provoke non equilibrium wave dynamics," in *The Ocean in Motion* (Springer, Cham, Switzerland, 2018), pp. 239–247.
[50]G. A. Athanassoulis, K. A. Belibassakis, and C. E. Papoutsellis, "An exact Hamiltonian coupled-mode system with application to extreme design waves over variable bathymetry," J. Ocean Eng. Mar. Energy **3**, 373–383 (2017).